https://doi.org/10.5194/egusphere-2026-2469
Preprint. Discussion started: 22 May 2026

A Cellular Automaton Model of Tropical Oceanic Rain Clusters with Criticality

Kevin K. W. Cheung[1], Chee-Kiat Teo[2], Tieh-Yong Koh[3,4]

[1]School of Atmospheric Physics, Nanjing University of Information Science and Technology, Nanjing, 210044, China
[2]Centre for Climate Research Singapore, 537054, Singapore (retired)
[3]Singapore University of Social Sciences, 599494, Singapore
[4]Department of Physics, National University of Singapore, 119077, Singapore

Correspondence to: Kevin Cheung (kevin.cheung@nuist.edu.cn)

Abstract. The distributions of the cluster area, A, and total rain rate, R, for tropical oceanic rain clusters from a cellular automaton (CA) are analysed for their scaling exponent ζ_A, ζ_R, and β where $f(s)\sim s^{-\zeta_S}; S \in \{A, R\}$; $f(s)$ the probability distribution of S. The CA only includes a few simple rules representing a small set of dynamics thought to be important for convective organization. These rules represent large-scale destabilization of the atmosphere under the moisture static energy framework with a slow driving timescale, as well as convective cells interaction through propagating gravity waves with a fast relaxation timescale. The CA exhibits percolation-like criticality, and the ζ_A is estimated to be near the 2-dimensional percolation value of 187/91. This agrees well with the ζ_A estimates over the Indian Ocean warm pool and the tropical Atlantic reported in previous modelling study. Although other critical exponents of the rain cluster distributions from the CA, namely the η_S (scaling exponent of characteristic scale with driving force) and D_S (cluster fractal dimension), $S\in(A, R\}$, depend on the adjustable parameter of the CA, the ζ_A is robust to the adjustable parameter. Although the CA cannot account for the observed $\zeta_A \sim 5/3$ reported elsewhere based on observations, further tuning of it such as through the convective cells interaction strength or manner may make it approach the state of self-organized criticality.

1 Introduction

It has long been recognized that clouds and rain possess the phenomenon of "clumping" (Randall and Huffman, 1980). In other words, clouds and rain seem able to self-organize or self-aggregate into clumps, more often referred to as clusters, from small convective cells, although such organization not necessarily implies reduction in complexity from the perspective of information entropy (see Li et al., 2019). With clumping, cloud cluster sizes follow power laws in form, $f(s)\sim s^{-\zeta_S}$, $f(s)$ being the distribution of some observables of the clouds or rain, S=s, and ζ_S a positive scaling exponent (López, 1977, 1978; Lovejoy, 1982; Cahalan and Joseph, 1989; Peters et al., 2009, 2010; Wood and Fields, 2011; O'Brien et al., 2013; Devineni et al., 2015; Traxl et al., 2016; Teo et al., 2017; Otsuka et al., 2017; Neggers et al., 2019; Li et al., 2022; Savre and Craig, 2023). Besides theoretical interests, recent studies also demonstrated that convection organization is a critical factor determining the

https://doi.org/10.5194/egusphere-2026-2469
Preprint. Discussion started: 22 May 2026

characteristics of extreme precipitation (Bao et al., 2017; Pendergrass, 2020; Semie and Bony, 2020; Roca and Fiolleau, 2020; Zhang and Wang, 2021) and tropical cyclogenesis (Muller and Romps, 2018).

It has been further suggested that tropical convective rain could be a critical phenomenon (Peters and Neelin, 2006; Peters et al., 2009; but cf. Muller et al., 2009), which provides a basis to understand what controls the power-law distributions seen in observations and models; If the tropical rain is indeed critical, then the exponent ζ_S for a certain observable would be universal – its value unique, and should be seen in the distributions across observations and numerical models, since the critical exponent is likely to depend only on a few fundamental physical constraints relevant to tropical moist convection, and not the detailed interactions and physical processes. Peters et al. (2009) suggests that tropical oceanic rain clusters behave geometrically like 2-dimensional percolation clusters (Broadbent and Hammersley, 1957), and consequently for the rain cluster area, $S = A$, $\zeta_A = 187/91$, in principle (Stauffer and Aharony 1994). Estimated value in Peters et al. from observations is about 2 appears to agree with percolation theory. Universality of observed rain clusters has been reported by Teo et al., 2017 (abbreviated as T17 hereafter) where the estimated ζ_A across the tropical basins are the same, but they reported a lower estimated value of $\zeta_A \sim 5/3$. Otsuka et al., (2017) through analysis of model rain clusters reported a power-law scaling for the rain cluster area when light rain is included and an exponent of 5/3 for the distribution of cloud shield area. Analysis of multi-year model rain clusters over the various different oceanic basins is needed for a more informed comparison with existing results in the literature.

In general, there are two approaches to investigate the self-aggregation processes and associated statistics of cloud/rain clusters. First is through dynamical modelling, often with Radiative Convective Equilibrium (RCE) and cloud-resolving resolution (Wing and Emanuel, 2014; Wing et al., 2017; Savre and Craig, 2023; Cerlini et al., 2023; Stephan and Stevens, 2025). The second is a "reductionist" approach that applies cellular automata (CA), which simplifies the physical and dynamical processes as deterministic or stochastic transition "rules" of lattice cell states in the model. With less computational resources necessary than in dynamical models, CA are able to study the critical behaviour of the observables represented in the models and facilitate comparison across a wide range of natural phenomena (Malamud and Turcotte 2000). Relevant to clouds and rain, CA models have been applied as part of convection parameterization schemes in numerical models to capture the stochastic nature of cloud organization (Palmer, 1997, 2001; Bengtsson et al. 2022; see also Nober and Graf, 2005; Graf and Yang, 2007). Previous applications of CA to study cloud clusters varied substantially in terms of how cloud processes are represented, although they are all fluid dynamics based. The early model of Nagel and Raschke (1992) focused on the interaction between cloud water vapor, humidity and vertical velocity represented in the model cells. Comparatively, the Silva et al. (2019) model is quite "realistic" in that it replicated condensation processes as well as advection by winds across the cells. Recently, the model in Najafi et al. (2021) and Cheraghalizadeh et al. (2024) also emulated microphysical processes in clouds and at the same time considered the cohesive energy of clouds resembling cell interaction in the Ising model.

In contrast to the aforementioned CA models, here we develop a CA based on atmospheric stability measured by the moist static energy (MSE; Yao et al. 2022). Our study is a step forward from previous observational analysis (T17) and model simulations (Teo et al. 2021, hereafter T21), which postulated rain clusters as avalanching sand-piles as in the self-organized criticality (SOC; Bak and Tang, 1987) theory. T17 and T21 analysed rain cluster distribution for its scaling exponents ζ_A, ζ_R

https://doi.org/10.5194/egusphere-2026-2469
Preprint. Discussion started: 22 May 2026

and β (for rain area, rain rate and area-conditioned rain respectively; See Appendix A for details). Our model exhibits feature similar to self-organized criticality (SOC) as what tropical rainfall could be (Peter and Neelin, 2006; Peters et al. 2009; Stechmann and Neelin, 2016; T17). Through such a CA model, we hope to elucidate the important factors that may cause the rain clusters to be critical, and its result would be useful in interpreting the distributions of the rain clusters seen in observations and numerical weather models.

The remaining of the paper is as follows: Section 2 introduces the CA for tropical oceanic rain cluster. Analysis of the model's cluster distributions is presented in Section 3. Further discussions on the implications of our findings are in Section 4 before summarizing our work in Section 5.

2 CA for tropical rain clusters

In this section, we give an overview of the CA for the tropical rain clusters use in this study. In the interest of clarity, the bulk of the physical basis of the model is presented in Appendix B. The rules of the CA are summarized in Table 1. The CA is defined on a square lattice with open boundaries. The main prognostic non-dimensional variable at each lattice site, X, represents the stability of the column of atmosphere against moist convection over a homogeneous ocean surface. In this simple model, X is taken to be the difference between the boundary-layer (below ~ 850 mb) averaged specific moist static energy, $h1$, and the layer-averaged specific saturated moist static energy at the top of the troposphere (above ~ 350mb), $h3^*$. By assuming that $h1$ and $h3^*$ are larger than the layer-averaged saturated specific moist static energy of the middle troposphere at all times, deep convection (and consequently precipitation) only occurs at a lattice site j if X_j is positive; no deep convection is triggered otherwise. In this model, X is bounded below at a value arbitrarily set to -1 representing a maximum stability the atmosphere can attain.

The CA operates in the following manner: At each time step t, X is increased by a predefined value d at all lattice sites, representing the large-scale destabilization of the atmosphere due to the combined effects of latent heat fluxes in the boundary layer, and also net radiative cooling of the atmosphere. For the unstable (toppling) sites with $X>0$, deep convection is assumed to restore the local stability, represented in the model by relaxing their X immediately back to some negative values. These relaxed X values are drawn stochastically from a distribution estimated from published literature (see Appendix B) to reflect the uncertainties introduce by various cloud processes during deep convection.

A raining (toppling) site in the model is assumed to interact with its neighbouring sites through two modes of horizontally propagating gravity waves excited by the latent heating profile at the site where the deep convection occurs. The first set of gravity wave, GW1, is excited at the mature stages of the deep convection when the maxima latent heating is at the mid-troposphere, while the second set of gravity wave, GW2, is excited at the later stage of the storm development when the heating maxima is higher up and presumably accompanied by evaporative cooling at the lower troposphere. These gravity waves are assumed to radiate horizontally away from the convective site with circular wave-front, with the phase speed of GW2 half of that of GW1 since the vertical wavelength of the earlier is taken to be about half of the latter. GW1 acts to stabilize the

https://doi.org/10.5194/egusphere-2026-2469
Preprint. Discussion started: 22 May 2026

atmosphere while the presence of GW2 acts to destabilize the atmosphere behind its wavefront. The effects of these gravity waves are represented in the CA by increasing X (destabilize) for the nearest-neighbours and decrease X (stabilize) for the next-nearest-neighbours of a toppling site (Eq. 5). The magnitude of the (de)stabilization of the (nearest-neighbour) next-nearest-neighbour is proportional to $|\Delta X|$ at the precipitating site with a tunable positive constant γ, which represents the degree of coupling between different locations by gravity wave dynamics.

Table 1: The rules for the CA on a square lattice with N grid points. The dynamic variables of the model, X, ΔX are functions of two time co-ordinates. t denotes the outer time (radiative timescale) while τ denotes the microscopic time (convective timescale). $\tau_F(t)$ is the final microscopic time at quiescence after the t^{th} avalanche, where $\tau_F(0) = 0$ by definition. g is a predefined random variable defined on [-1,0] as the X attained after toppling whose distribution is shown in Figure B2. Eqs. (3) and (4) represent the relaxation process to stable condition after toppling. Refer to Appendix B for the physical basis for the equations.

***Homogeneous drive*:**

$$X_j(t,0) = X_j(t-1,\tau_F(t-1)) + d;\ \ ,\forall\, j = 1,\cdots,N;\ d\ > 0;\ t = 1,2,\cdots \tag{1}$$

***Toppling*:**

If $X_j(t,\tau) \geq 0$,

$$X_j(t,\tau+1) \sim g(y),\ \tau = 0,1,2,\cdots \tag{2}$$

and

$$I_j(t,\tau) = I_j(t,\tau-1) - \Delta X_j(t,\tau);\ \ \tau \geq 1 \tag{3}$$

where

$$\Delta X_j(t,\tau) = X_j(t,\tau+1) - X_j(t,\tau) \leq 0 \tag{4}$$

Interaction:

$$X_k(t,\tau+1) = \begin{cases} \max\{X_k(t,\tau) + \frac{1}{12}\gamma\Delta X_j(t,\tau), -1\} - \frac{3}{4}\left(\frac{1}{4}\gamma\right)\Delta X_j(t,\tau) & k \in \{m\,|\,|r_m - r_j| \leq 1, m \neq j\} \\ \max\{X_k(t,\tau) + \frac{1}{12}\gamma\Delta X_j(t,\tau), -1\} & k \in \{m\,|1 < |r_m - r_j| \leq 2, m \neq j\} \end{cases} \quad \gamma > 0 \tag{5}$$

Cluster rain rate:

At quiescence, let J_n be the set of lattice indices the defines the n^{th} cluster, $a_n = \|J_n\|$ its area, $P_n = \sum_{j\in J_n} I_j$ its avalanche intensity. The corresponding cluster rain rate is

$$r_n = k(a_n)P_n; k(a) = a^{\beta-1};\ \beta = 4/3 \tag{6}$$

Parallel update during the avalanche (when toppling activities in the CA are still happening) is enforced – all the sites excited (X>0) at a microscopic time step, τ, will only be relaxed at the next microscopic time, τ+1. Driving of the model resumes only after quiescence (X<0 at all sites) ensuring the clear separation between the driving (synoptic) and relaxation (convective) time

https://doi.org/10.5194/egusphere-2026-2469
Preprint. Discussion started: 22 May 2026

scale. Multiple relaxations or back-toppling, at a given site are permitted in the model. The rain clusters are identified at quiescence as the collection of sets of rainy sites connected with their nearest neighbours. As the model is analysed in its stationary state, how the model is initialized is irrelevant.

Originally, we envisaged that some non-trivial scaling relation between the cluster rain rate (taken as proportional to the avalanche intensity) and the cluster area would naturally emerge from the model. However, we find that the avalanche intensity from the CA is effectively proportional to the cluster area on the average, perhaps due to lack of representation of the detail MCS circulation necessary to reproduce mesoscale cluster with area-dependent rain intensity as discussed in T21. As such the cluster total rain rate of a CA cluster after quiescence is computed by Eq. (6), as a product of the total avalanche intensity of the cluster with a cluster size-dependent coefficient k. Eq. (6) constrains the CA to reproduce the required observed scaling of E(R|a) for mesoscale clusters (T17).

Although the CA shares some common features to some known SOC models like the Olami-Feder-Christensen (OFC) model (Olami et al., 1992), namely the existence of a toppling threshold; homogeneous external drive; and the clear separation of slow driving and fast relaxation time scales, it is not an SOC model. To understand the reason why, we note that according to the Absorbing State Mechanism (ASM; Dickman et al., 1998; Vespiganni and Zapperri, 1998), the CA can potentially exhibit SOC only if it has a vanishingly small dissipation coefficient, ε, defined in the case for the CA, as ratio of the net loss in X through its interaction with its neighbours per unit change in X, as a result of a single toppling. If we ignore, for simplicity, the lower bound constrain imposed on X, the total change in X at the twelve neighbours of a toppling site away from the boundaries (the four nearest-neighbours and eight next-nearest-neighbours of the toppling site) is $\gamma\Delta X - 4 \times \frac{3}{16}\gamma\Delta X = \frac{1}{4}\gamma\Delta X$ (Eq. 5). This means that $\varepsilon = 1 + \frac{1}{4}\gamma \geq 1$, since $\gamma \geq 0$. As a model for tropical convection, this is not unreasonable since deep convection have a net stabilizing effect on the atmosphere. However, as discussed in detail in the next section, the CA still exhibits critical behaviour for unique value of d for a given γ.

3 Cluster distributions from CA

3.1 Two-dimensional site percolation

Since CA depends on the two adjustable parameters, γ and d, we denote CA with the coupling constant γ, driven with a magnitude d, as $CA_{\gamma,d}$ for brevity. For example, $CA_{0,d}$ has the meaning of the CA with $\gamma = 0$, and with an instability of magnitude d added to each lattice sites at each driving cycle (Eq. 1).

The phase space for CA as a function of γ and d is represented schematically in Fig. 1. For $0 \leq \gamma \leq 2.5$, the cluster distributions are found to follow the scaling ansatz similar in form to the 2-dimensional site-percolation (e.g., Christensen and Moloney, 2005) when d approaches a critical value (d_c):

https://doi.org/10.5194/egusphere-2026-2469
Preprint. Discussion started: 22 May 2026

$$f_S(s) \propto \begin{cases} s^{-\zeta_S}\mathcal{G}_S\left(\frac{s}{\xi_S^{D_S}}\right) & d \longrightarrow d_c, a \gg 1, Z \gg \xi_A \\ s^{-\zeta_S}\tilde{\mathcal{G}}_S\left(\frac{s}{Z^{D_S}}\right) & d \longrightarrow d_c, a \gg 1, 1 \ll Z \ll \xi_A \end{cases} \quad (7)$$

where $f_S(S)$ is the discrete probability distribution $P(a)$ when S is A and $f_S(s)$ is the probability density function, $f(r)$, when S is R; $\mathcal{G}_S(x)$ and $\tilde{\mathcal{G}}_S(x)$ are the scaling functions for the two different ξ_A regimes, but share the same generic property of approaching to some non-zero constants when $x \ll 1$ and decays rapidly when $x \gg 1$; ξ_S is the characteristic "length scale" of the cluster and the D_S is the a γ-dependent exponent for the distributions; d_c a γ-dependent value of d where the CA is critical when $d = d_c$. When S is A, ξ_A has the meaning of a geometric length scale of the cluster (e.g., the averaged radius of gyration of the clusters; Cheraghalizadeh et al. 2024) and based on which separating the two scaling regimes in Eq. (7); D_A, the cluster fractal dimension and $\xi_A^{D_A}$, the characteristic cluster area. Similarly, $\xi_R^{D_R}$ is the characteristic cluster total rain rate. Furthermore, the characteristic scale scales as

$$\xi_S^{D_S} \propto |d - d_c|^{-\eta_S}, S = \{A, R\}, \quad (8)$$

where η_S is a γ-dependent exponent.

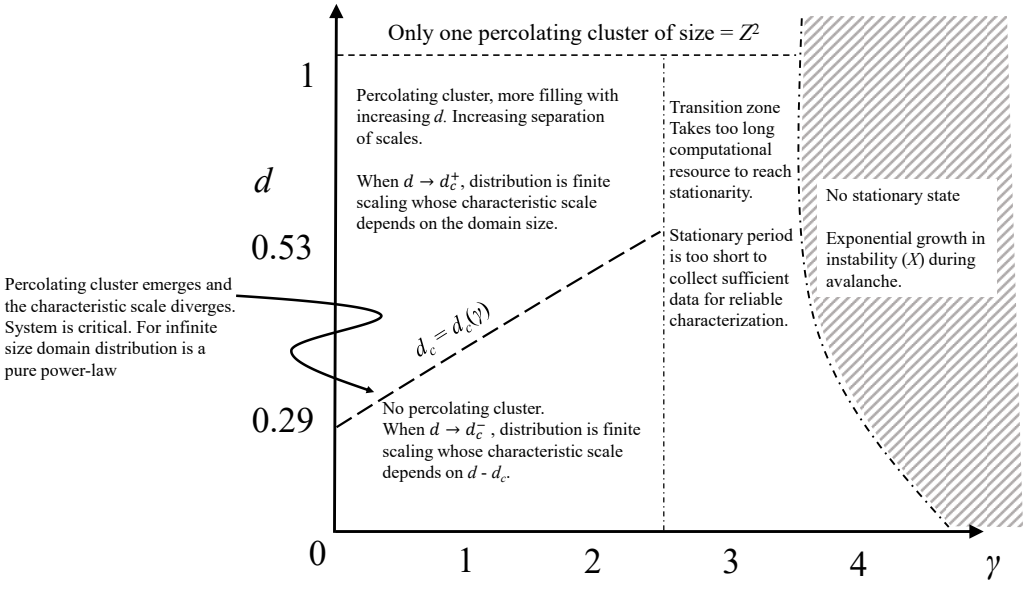

Figure 1: Schematic representation of the phase space of CA as a function of the drive magnitude *d* and the coupling constant *γ*.

https://doi.org/10.5194/egusphere-2026-2469
Preprint. Discussion started: 22 May 2026

3.2 Non-interacting lattice

The motivation of the CA scaling ansatz can be most easily inferred from the case when $\gamma = 0$. For $CA_{0,d}$, there is no interaction amongst the lattice sites; whether a site become unstable ($X>0$) after adding d units during its driving phase, depends only on its antecedent value of X. In its stationary state, the probability that a lattice site becomes unstable after being driven is equal to the ensemble mean of the fractional area coverage of the rain clusters, Ω. Hence $CA_{0,d}$ can be map to the 2-dimensional site percolation on a square lattice of the same length, Z, with the probability of occupancy probability, $p = \Omega(d)$. This claim is supported by Fig. 2 where the cluster size distributions for $CA_{0,d}$ being practically indistinguishable from the sample cluster size distributions of a 2-dimensional site-percolation with the estimated Ω of the $CA_{0,d}$ chosen as p. For Fig. 2b, the drive d for the $CA_{0,d}$ is set to approximately its critical value such that $\Omega(d = d_c = 0.2901) \approx p_c = 0.5928$. This value of d_c is determined from preliminary experiments based on a $Z = 128$ lattice.

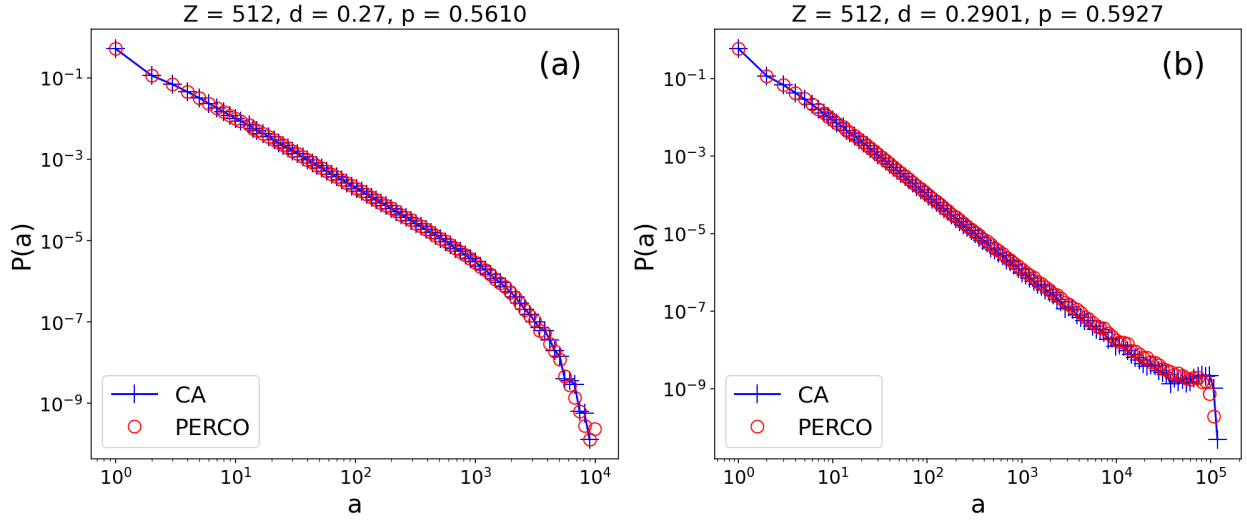

Figure 2: Probability distributions of the cluster size (cross) for $CA_{0,0.27}$ (a) and $CA_{0,0.2901}$ (b) for $Z = 512$, together with the cluster size distributions from a 2-dimensional site percolation on a square lattice (open circle) of the same size with occupancy probability p set to the mean averaged fractional rain cluster coverage, Ω, for the CA. Approximately 10^7 clusters are used to sample the probability distributions.

For the standard site-percolation with occupancy probability $p = p_c$, the system becomes critical, and the characteristic cluster length scale, ξ_A, diverges. At criticality the system transit to percolation, that is, an incipient infinitely large cluster emerges in the limit of an infinitely large domain, and $P(a) \propto a^{-\zeta_A}$ for $a \gg 1$, with $\zeta_A = 187/91$. For standard site-percolation, the characteristic cluster area, $\xi_A^{D_A} \propto |p - p_c|^{-\eta_A}$ with $\eta_A = 91/36$ (Stauffer and Aharony 1994). Since $p = \Omega(d)$ for $CA_{0,d}$, $\xi_A^{D_A} \propto |\Omega(d) - \Omega(d_c)|^{-\eta_A} \approx \left(\Omega'(d_c)\right)^{-\eta_A} |d - d_c|^{-\eta_A}$ to a first approximation, $\Omega'(d_c)$ (>0) being the first order derivative of Ω evaluated at d_c. On the other hand, when $Z \ll \xi_A$, the distribution is *finite-size scaling* and the characteristic cluster area becomes proportional to Z^{D_A} instead. We will call the scaling ansatz when $Z \gg \xi_A$ simply as finite scaling to differentiate from finite-size scaling ansatz for clarity.

https://doi.org/10.5194/egusphere-2026-2469
Preprint. Discussion started: 22 May 2026

The finite scaling and finite-size scaling of $CA_{0,d}$ cluster size distributions is demonstrated in Fig. 3. The d values are judiciously selected such that $Z \gg \xi_A(d)$ (Fig. 3a). As d approaches d_c (~ 0.2901), ξ_A increases rapidly and consequently the interval of cluster area where $P(a)$ exhibits a power-law form becomes increasingly discernible. On the other hand, $\xi_A(d = 0.2905)$ is much larger than $Z \leq 512$, and Fig. 3b is suggestive of finite-size scaling of $P(a)$ for $Z \leq 512$.

Since the scaling function $\mathcal{G}_A$ ($\tilde{\mathcal{G}}_A$) is identical in principle, across the different d (Z), the scaling ansatz (Eq. 7) can be tested directly using data collapse, i.e., plotting together the scaling functions inferred separately for the different distributions in Figs. 3a, b. The inferred scaling functions, $\hat{\mathcal{G}}_A$ for the different d values are shown in Fig. 3c, where the reweighted probabilities, $a^{-\hat{\zeta}_A}P(a)$, are plotted against the $x = a/(\hat{d}_c - d)^{-\hat{\eta}_A}$. Note that hatted symbols denote the estimates. The methods used to obtain these estimates are described in Appendix C. $\hat{\eta}_A$ = 2.689 ± 0.067 is slightly larger than the expected theoretical value of 91/36 = 2.528, while $\hat{\zeta}_A$ = 1.914 ± 0.095 is in agreement with the theoretical value of 91/87 ≈ 2.055. The inferred scaling functions associated with the $P(a)$ for the different d values collapse together well for $x \gtrsim 10^{-2}$. For small x (e.g., $x \lesssim 10^{-4}$ for the $\hat{\mathcal{G}}_A$ with d = 0.28) finite scaling is no longer valid as the cluster distribution would then depends on the details of CA. As d approaches d_c, ξ_A increases rapidly (Eq. 8). Therefore the lower limit of x where the finite scaling breaks down decreases, evident from the decrease in the x where the overlap of the inferred scaling function beings as d approaches d_c (compare the x where $\hat{\mathcal{G}}_A$ with d = 0.28 collapse with the $\hat{\mathcal{G}}_A$ with d = 0.27, and with d = 0.25 in Fig. 3c). Similar inferences for the scaling function $\tilde{\mathcal{G}}_A$ is performed when the distribution is finite-size scaling ($Z \ll \xi_A$), with d = 0.2905 as shown in Fig. 3d. Note that as the scaling ansatz in Eq. 7 is defined for finite clusters, the percolating clusters from the numerical simulation are excluded when sampling the clusters. Details of the methods used in estimating D_A and ζ_A are in Appendix C. $\widehat{D}_A$ = 1.954 ± 0.057, slightly larger than the theoretical value of 91/48 ≈ 1.896 while $\hat{\zeta}_A$ = 2.084 ± 0.189 agrees with theoretical value of ζ_A.

The scaling characteristics for the $CA_{0,d}$ cluster total cluster rain rate distributions are similar to that describe above for the cluster size distributions. Figures 4a, b shows the R-distributions when they are finite scaling and finite-size scaling respectively. Away from $r \sim 1$, the increasingly discernable power-law form of $f(r)$ for $r > 1$ when d approaches d_c (Fig. 5a) and with increasing Z (Fig. 5b) are reminiscent to what is observed for $P(a)$. The collapses of the distribution in the two scaling regimes are shown in Figs. 4c, d, using $\hat{\zeta}_R$ = 1.724 ± 0.103, $\hat{\eta}_R$ = 3.742 ± 0.088, $\widehat{D}_R$ = 2.596 ± 0.073 and d_c =0.2925 ± 0.0005 estimated using the same method used in obtaining the exponents for A (see Appendix C). The exponents for R are not independent from those of A due to the constrain $E(R|a)$ α a^{β} imposed by the CA (Eq. 6 and Appendix A): ζ_A and ζ_R are related with β by the scaling relation (Eq. A4) as a result of the constrain (e.g., Prussner, 2012). Estimate of β from the scaling relation $\hat{\zeta}_A$ and $\hat{\zeta}_R$ is 1.380 ± 0.338 which is consistent with the imposed value of 4/3. In addition, D_R and D_A area related as follows: The characteristic scale for $R \sim Z^{D_R}$ which scales as $E(R|Z^{D_A}) \sim Z^{\beta D_A}$. Since the relation is true for all Z ($1 \ll Z \ll \xi_A$), then $D_R = \beta D_A$. Similarly, one can demonstrate through Eq. (8) that $\eta_R = \beta\eta_A$, $\frac{\hat{\eta}_R}{\hat{\eta}_A}$ = 1.3959 ± 0.0675 and $\frac{\widehat{D}_R}{\widehat{D}_A}$ = 1.3348 ± 0.0763 consistent with the imposed β = 4/3.

https://doi.org/10.5194/egusphere-2026-2469
Preprint. Discussion started: 22 May 2026

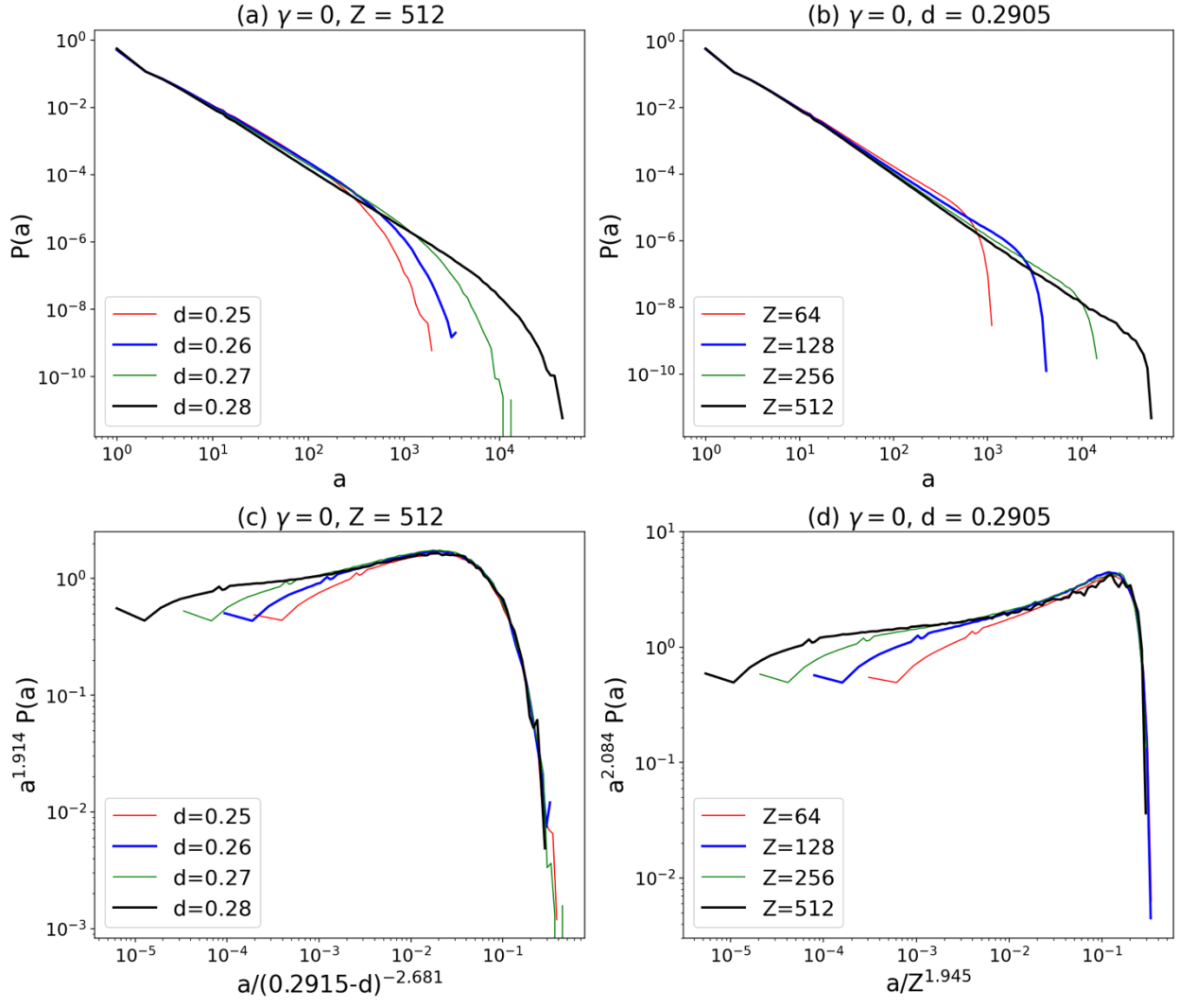

Figure 3: (a) Cluster size distributions for $CA_{0,d}$ with $Z = 512$ and d from 0.25 to 0.28 with increment of 0.01 (b) As (a) but with $Z = 64$, 128, 256 and 512 for $CA_{0,0.2905}$. Note that the percolating clusters (largest cluster from each avalanche) are excluded in this case. (c) The data collapse for the distributions shown in (a) using estimated values for τ_A, η_A and d_c (see main text), (d) Same as (c) but shows the data collapse for the distributions shown in (b). Approximately 4×10^7 clusters are used to sample each distribution shown in the plots.

https://doi.org/10.5194/egusphere-2026-2469
Preprint. Discussion started: 22 May 2026

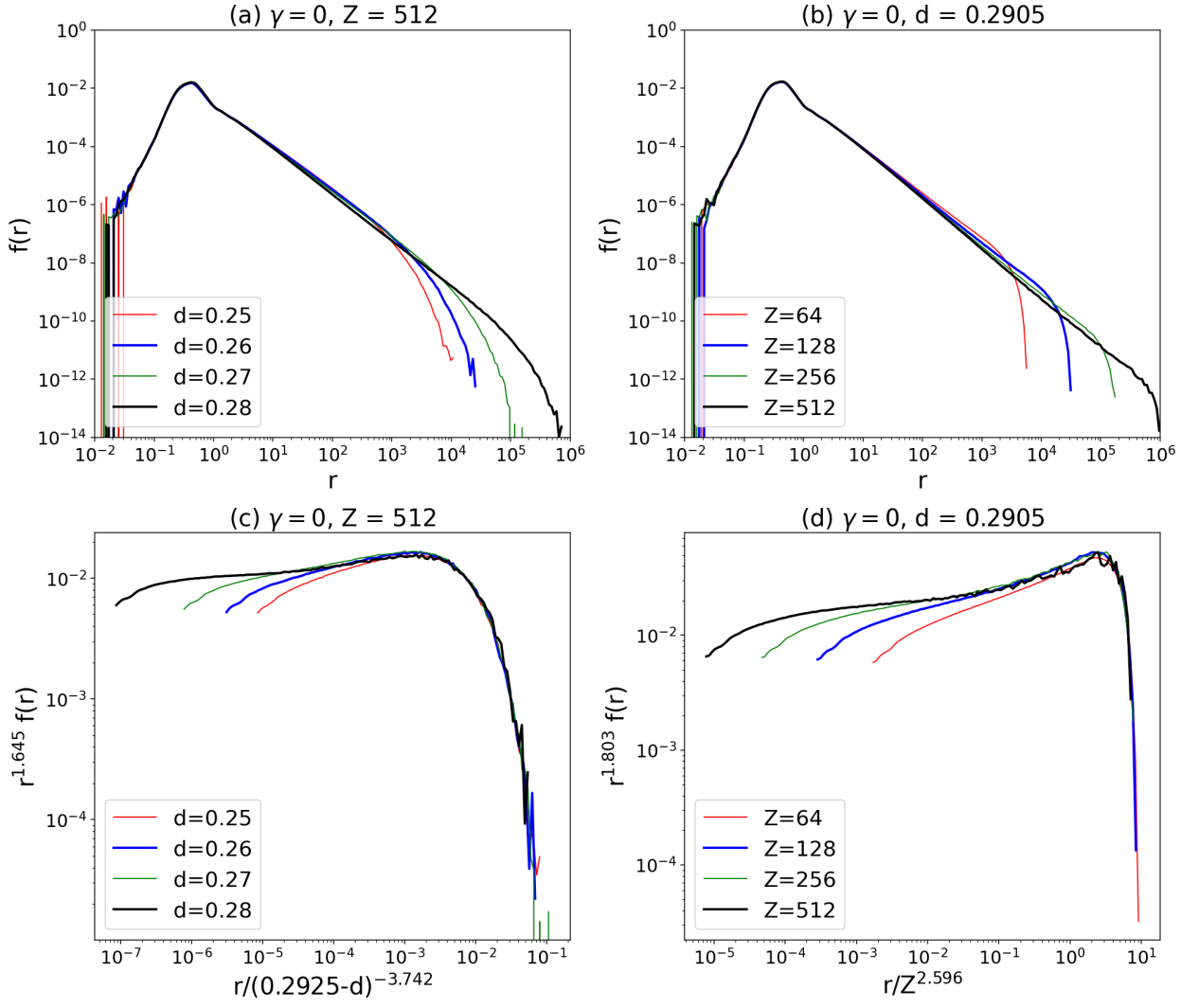

Figure 4: As in Figure 3 but for the distributions of the cluster total rain rate. Note the very small *f*(*r*) values for small *r* in panels (a) and (b), which are due to the single-cell clusters in the model that toppled during simulation and contributed to the pdf.

https://doi.org/10.5194/egusphere-2026-2469
Preprint. Discussion started: 22 May 2026

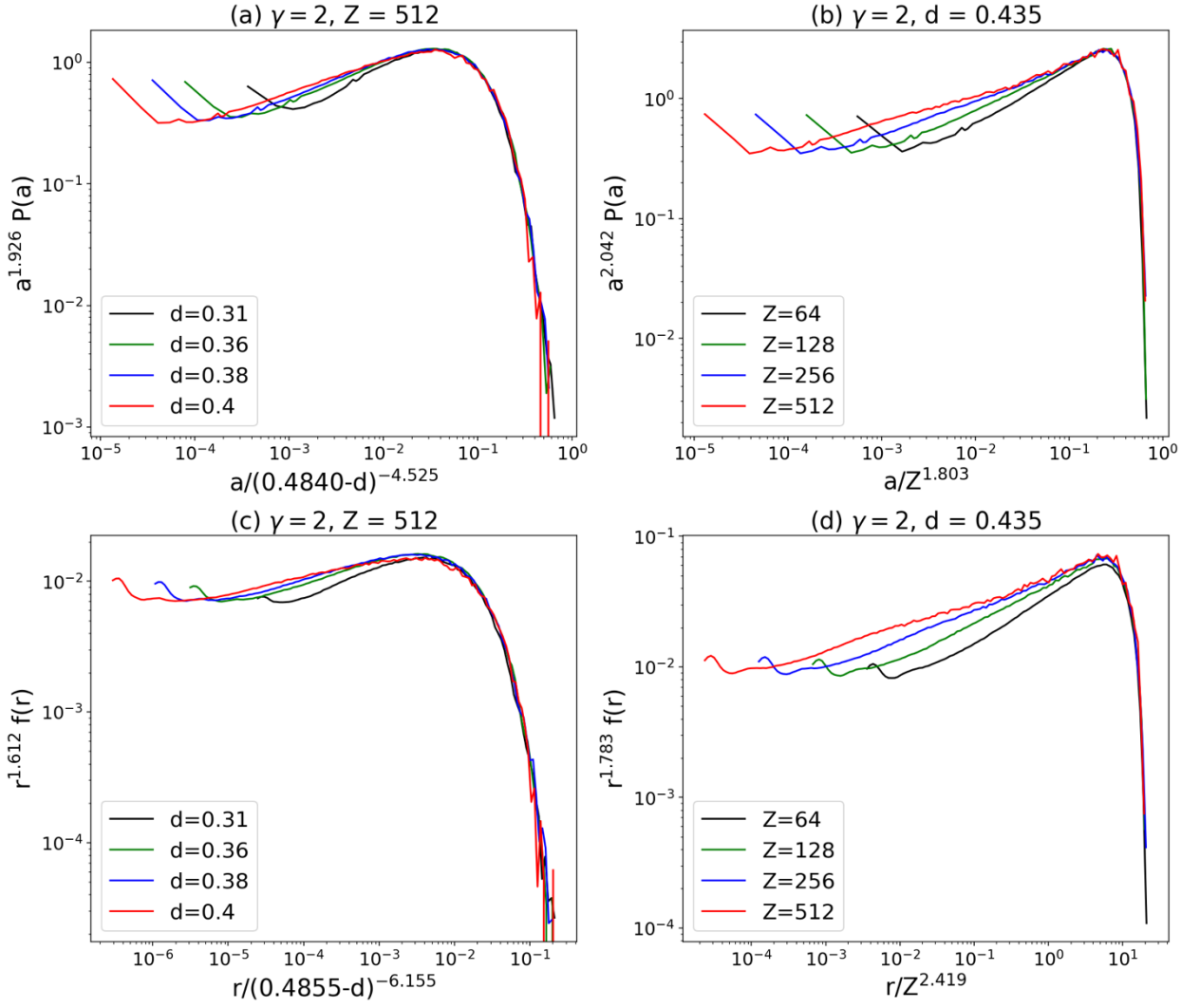

220 **Figure 5: As in Figures 3c, d and 4c, d but for γ =2 with d = 0.31, 0.36, 0.38 and 0.40 for (a) and (c) and d = 0.435 for (b) and (d).**

3.3 Interacting lattice

The finite scaling ansatz holds as well for the distributions of $CA_{\gamma,d\to d_c}$ for $0 < \gamma \leq 2.5$, albeit the following generalizations from $CA_{0,d\to d_c}$ (Fig. 6 and Table 2): 1) d_c and η_S are increasing functions of γ; 2) D_S is a decreasing function of γ. The method
225 of obtaining the scaling exponents and d_c for each of γ tested are the same as the preceding discussion on $CA_{0,d}$ (Appendix C). For example, Figs. 5c, d show reasonable data collapse for the two finite scaling regimes $Z \gg \xi_A$ and $1 \ll Z \ll \xi_A$ for $CA_{\gamma,d}$ for the case when $\gamma = 2$, using estimates of ζ_S, η_S and D_S and d_c. Similar data collapse with their corresponding scaling exponents estimates are also obtained for γ = 0.5, 1, 1.5 and 2.5 (not shown).

https://doi.org/10.5194/egusphere-2026-2469
Preprint. Discussion started: 22 May 2026

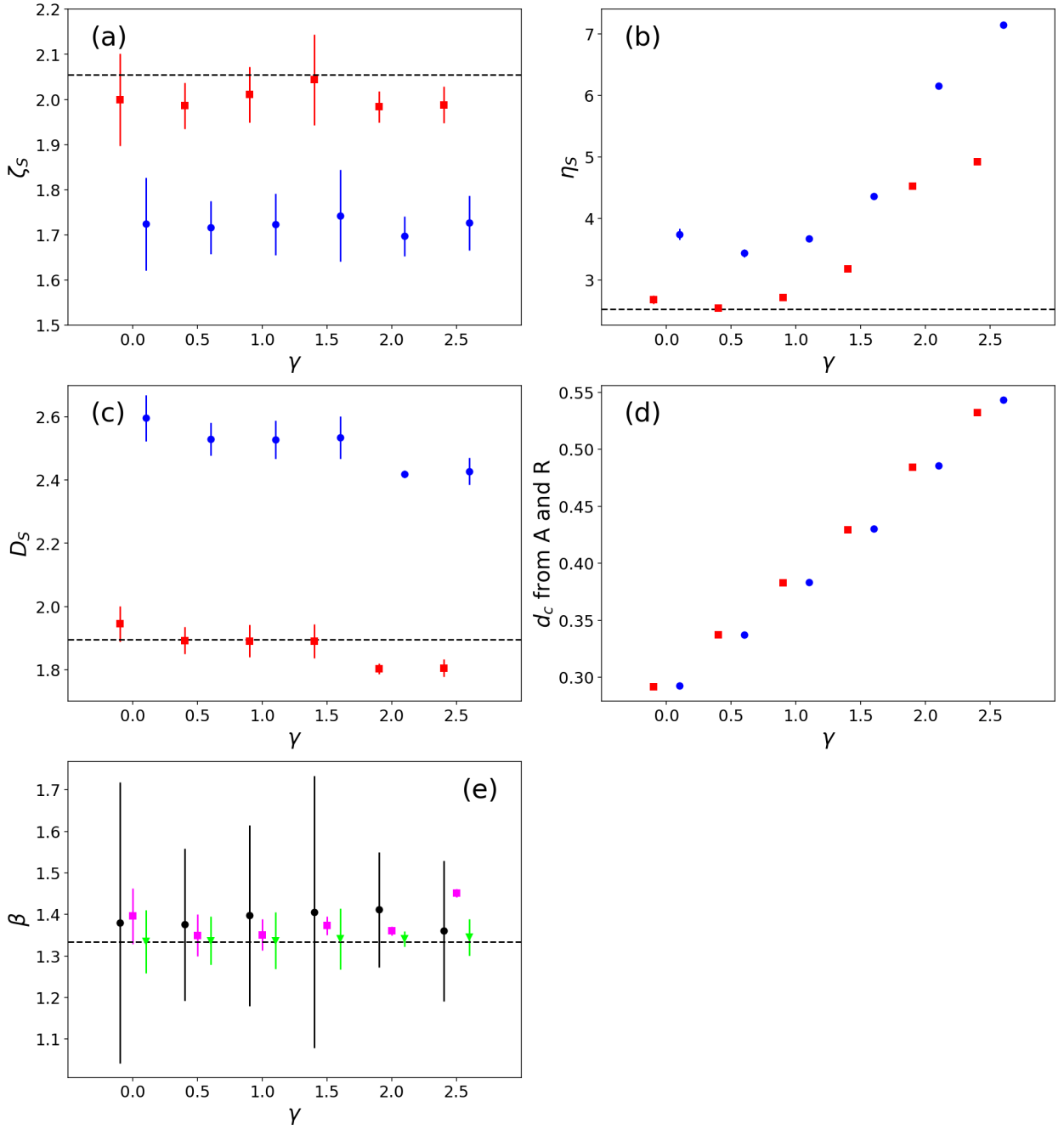

230 **Figure 6: (a) – (d) Plots of the various estimated scaling exponents and d_c in Table 1 for the distribution for A (red) and R (blue). The dashed horizontal lines are the corresponding values from 2-dimensional site-percolation. (e) β estimated from the scaling relation (equation A4; black circle), $\frac{\widehat{\eta}_R}{\widehat{\eta}_A}$ (magenta square); $\frac{\widehat{D}_R}{\widehat{D}_A}$ (lime inverted triangle). Dash line is the expected $\beta = 4/3$.**

https://doi.org/10.5194/egusphere-2026-2469
Preprint. Discussion started: 22 May 2026

Table 2: Numerical estimates of the various scaling exponents and critical values for the *A* and *R* distributions for the CA. The corresponding theoretical scaling exponents for the 2-dimensional site-percolation are listed in the last column for reference. The last row is the expected β from the scaling relation (Eq. A4).

	γ	0	0.5	1	1.5	2	2.5	percolation
$\hat{\zeta}_S$	*A*	2.000 ± 0.200	1.986 ± 0.100	2.011 ± 0.121	2.044 ± 0.197	1.984 ± 0.068	1.988 ± 0.078	2.055 (187/91)
	R	1.724 ± 0.103	1.717 ± 0.059	1.724 ± 0.069	1.743 ± 0.102	1.697 ± 0.044	1.727 ± 0.061	
$\hat{\eta}_S$	*A*	2.681 ± 0.067	2.545 ± 0.038	2.717 ± 0.038	3.178 ± 0.027	4.525 ± 0.019	4.921 ± 0.018	2.528 (91/36)
	R	3.742 ± 0.088	3.434 ± 0.064	3.670 ± 0.051	4.363 ± 0.036	6.155 ± 0.025	7.141 ± 0.024	
$\hat{D}_S$	*A*	1.945 ± 0.057	1.893 ± 0.043	1.891 ± 0.051	1.891 ± 0.054	1.803 ± 0.016	1.805 ± 0.028	1.895 (91/48)
	R	2.596 ± 0.073	2.530 ± 0.052	2.528 ± 0.060	2.535 ± 0.067	2.419 ± 0.011	2.428 ± 0.043	
$\hat{d}_c$	*A*	0.2915 ± 0.0005	0.3370 ± 0.0005	0.3830 ± 0.0005	0.4295 ± 0.0005	0.4840 ± 0.0005	0.5320 ± 0.0005	
	R	0.2925 ± 0.0005	0.3370 ± 0.0005	0.3835 ± 0.0005	0.4305 ± 0.0005	0.4855 ± 0.0005	0.5435 ± 0.0005	
$\hat{\beta}$		1.3333 ± 0.0001	1.3337 ± 0.0002	1.3348 ± 0.0005	1.3373 ± 0.0013	1.3398 ± 0.0018	1.3413 ± 0.0024	
$\tilde{\beta}$		1.380 ± 0.338	1.376 ± 0.183	1.397 ± 0.217	1.406 ± 0.328	1.411 ± 0.139	1.360 ± 0.170	

d_c increases with γ since the net instability being removed by a convection event (toppling) depends linearly on γ. Hence as γ increase, the magnitude of d needed to drive the model to criticality increases linearly as well (Fig. 6d). D_A is a decreasing function of γ since the suppression of convection by GW1 becomes stronger with increasing γ. Hence, we might expect that the CA rain clusters to be increasingly riddled with "holes" and consequently, their fractal dimension which D_A represents decreases. As expected, D_R and η_R appears to be simply an amplification of D_A and η_A respectively, since the imposed scaling of E(R|A) in the CA constrains the ratio of D_R/D_A and η_R/η_A to be β. Figure 6e shows that the expected relation is well reproduced in the CA for D_R and D_A, but not as well for $\gamma \geq 1.5$ for η_R and η_A. The estimates of ζ_A, ζ_R and β for the CA also satisfy the scaling relation Eq. (A4) for all γ tested.

In contrast with η_S and D_S, ζ_S appear to be insensitive to γ for $\gamma \leq 2.5$, with an average value of 2.003 ± 0.058 for $\hat{\zeta}_A$, which agrees with the exponent for percolation (187/91) and 1.721 ± 0.067 for $\hat{\zeta}_R$. Whether the true ζ_A for the CA is identical to that of the 2-dimensional site-percolation (187/91) when $\gamma > 0$ remains to be explained. The site interactions due to the gravity waves would have introduced a degree of spatial correlation of X over the domain and hence, $CA_{\gamma>0,d}$ would not have a one-to-one correspondence with the 2-dimensional site-percolation, as evident from the deviations of $\hat{\eta}_A$ and $\hat{D}_A$ from the percolation values with increasing γ. On the other hand, $\hat{\zeta}_A$ for $\gamma > 0$ are the same across within their error estimates from our analysis (Table 2 and Fig. 6a). Although $\hat{\zeta}_A$ for γ = 0.5, 2 and 2.5 is significantly different from the expected value for 2-dimensional percolation of 187/91, we note that for γ = 0, the *point estimate* for ζ_A is ~ 0.055 less than 187/91 as well. The possible reason behind the discrepancy could be that although care has been taken in allowing a fairly large range of ξ_A and Z to probe the scaling functions in our present analysis, the number of clusters used ($\mathcal{O}(10^7)$) to probe scaling function for the

https://doi.org/10.5194/egusphere-2026-2469
Preprint. Discussion started: 22 May 2026

larger domain sizes (Z = 128, 512) may still be insufficient, and contributes to the biases in the point estimates. The value of 187/91 would be within the prediction interval of all the $\hat{\zeta}_A$ for $\gamma > 0$ if adjusted for similar magnitude of underestimates.

As d increases towards unity beyond d_c, the percolating cluster becomes increasingly space-filling. Since the finite clusters can only exist in the gaps of the percolating cluster, the sizes of the finite clusters decrease rapidly with the increasing d. Consequently, on a probability plot such as those shown in Fig. 7, the frequency of clusters of size in the order of the domain size increases rapidly with d, while the characteristic size of the finite clusters decreases rapidly. When $Z \gg \xi_A(d)$, as the case for d = 0.42 and 0.6 for γ = 0 and γ = 2 respectively in the figure, there is a clear separation of scales in the cluster size distribution. When d is unity, there is only one trivial (percolating) cluster of $a = Z^2$.

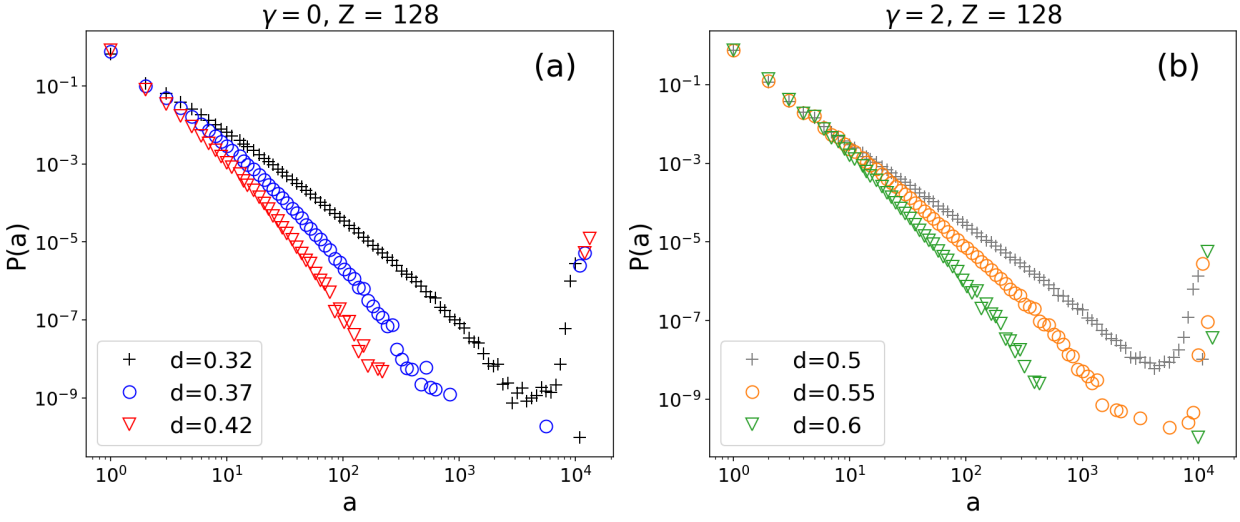

Figure 7: CA sample cluster size distributions for large d values (relative to d_c) using a domain size Z = 128. (a) γ = 0 with d = 0.32 (black crosses), 0.37 (blue circles) and 0.42 (red triangles) (b) γ = 2 with d = 0.50 (gray crosses), 0.55 (orange circles) and 0.60 (lime triangles). About 10^7 clusters are used to sample each probability distributions.

For increasing γ beyond 2.5, CA takes increasing time to reached stationarity and hence we do not have sufficient sample size to fully characterize the distribution. For $\gamma > 4$ the CA the domain averaged instability, X, is found to increase exponentially as the numerical simulation progresses, even with $d \ll 1$. The reason behind such a behavior in the CA is because the amount of instability that can be removed at each of the lattice sites behind the GW1 wavefront is constrained by the minimum that X can attain (-1), while X behind the GW2 wavefront (the nearest neighbours of a relaxing site) is not bounded above (Eq. 5). Hence for large enough γ, the total change in X after a toppling can be positive which represents a deep convection rain processes that introduce net instability to the atmosphere instead of stabilizing the atmosphere. As such we regard such model configuration as non-physical and choose not to analyse the model in these large γ regime.

The β estimates analysed from the CA cluster samples (Table 2 and Fig. 7) are close to 4/3 as expected. The procedure of estimating β for each γ tested ($\gamma \in \{0, 0.5, 1, 1.5, 2, 2.5\}$) is similar to that carried out for in T21. The only difference from T21

https://doi.org/10.5194/egusphere-2026-2469
Preprint. Discussion started: 22 May 2026

is that for the CA, b in the Eq. (2) is modelled as a linear function of $1/Z$, following T17, as shown in Fig. 8a using the case when $\gamma = 2$ by way of an example. From Fig. 8b, β appears to be an increasing function of γ. This is because with increasing γ, the occurrence of multiple toppling at a given lattice site may have increased for larger clusters resulting in a slight dependence of the avalanche intensity with the cluster area.

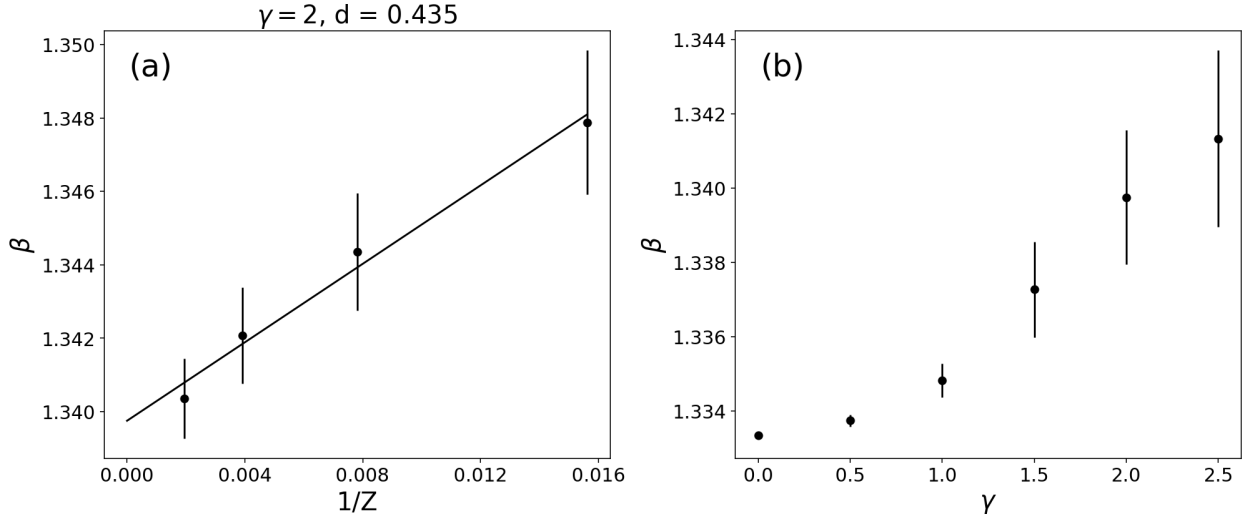

Figure 8: Estimates of β for the CA. (a) The linear regression model to estimate β for $CA_{2,\,0.4532}$ using the various β $(1/Z)$ (Eq. A3), where the regression intercept is taken as $\widehat{\beta}$. (b) Estimated β as a function of γ. The error bars in both plots are the 95% confidence interval of the regression estimates.

4 Discussions

Although the CA exhibits criticality, the ζ_A is different from the observed value of about 5/3 reported in T17. From the results in the preceding section, adjusting the value of γ does not change the ζ_A, although the other critical exponents, η_A and D_A changes with γ. The robustness of the ζ_A lies perhaps more in the dynamics represented by the toppling mechanism in the CA; If we assume that only the destabilization in the vicinity of deep convection by GW2 is the main mechanism behind the rain clusters organization, the CA can be further simplified by excluding the effects of stabilization of the atmosphere by GW1 in Eq. (5). Following the discussion in section 2, the dissipative coefficient, ε, for this simplified CA, call it sCA, would be $\varepsilon = 1 - \frac{3}{4}\gamma$. By the Absorbing State Mechanism, sCA may potentially exhibit SOC if $\gamma \to 4/3$ (i.e. $\varepsilon \to 0$) and $d \to 0^+$. In fact, $sCA_{\gamma,0^+}$ (the subscripts having the same meaning as the preceding section) is similar to the OFC model (Olami et al., 1992), in terms of its rules for nearest-neighbour interactions, γ as a control of the level of non-conservation, as well as how the model is driven. The OFC model is widely accepted to be an SOC when bulk conservation is enforced (i.e. $\varepsilon = 0$; Bröker and Grassberger, 1997; Chabanol and Hakim, 1997; De Carvalho and Prado, 2000). Indeed, preliminary survey with a set of small domain experiments indicates that $sCA_{4/3,0^+}$ is a SOC (Fig. 9), with $\zeta_A \approx 1.35$. We use the bulk driving scheme of the OFC model (Olami et al., 1992) to achieve the vanishing drive ($d \to 0^+$) for this set of experiment. When $\gamma = 0$, $sCA_{0,d}$ also exhibits

https://doi.org/10.5194/egusphere-2026-2469
Preprint. Discussion started: 22 May 2026

critically at $d = d_c \approx 0.292$ with ζ_A =187/91 since it is equivalent to $CA_{0,d}$ whose cluster size distribution is in turn, equivalent to the cluster size distribution of the 2-dimensional site-percolation. The behaviour of $sCA_{4/3,0^+}$ and $sCA_{0,d}$ lead us to suspect that in general, for any $\gamma \in (0, 4/3)$, there exist a $d = d_c(\gamma)$ where sCA_{γ,d_c} exhibits criticality, and unlike the case for the CA, ζ_A could be a function of γ as well. We represent our hypothesis in Fig. 9c. Note that $\varepsilon < 0$ for $\gamma > 4/3$ and hence sCA cannot
305 achieve statistical stationarity for $\gamma > 4/3$. We feel that the sCA is a cell-automata which may exhibit critical phenomena, and at the same time "tunable" via γ to reproduce the observed $\zeta_A \sim 5/3$. Indeed, some finitely driven cellular automata are reported to display varying power-law exponents in their event size distributions (Piegari et al., 2006).

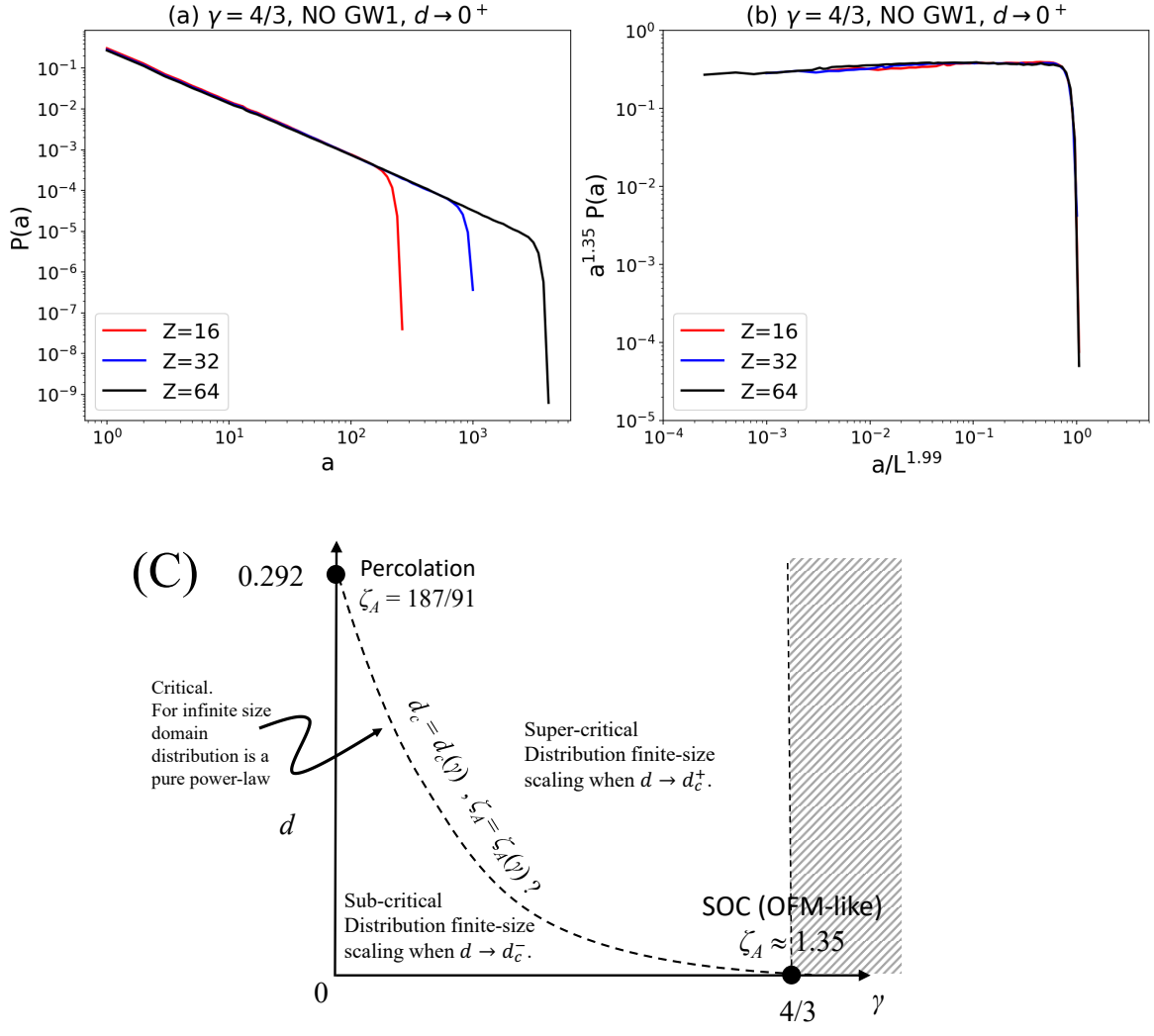

310 **Figure 9: Characteristics of the sCA (CA excluding the representation of the GW1 dynamics in its toppling mechanisms. (a) The distribution of cluster area for different domain size (Z = 16, 32, 64) and (b) its data collapse for the sCA with $\gamma = 4/3$ and with $d \to 0^+$. (c) Schematic illustrating the hypothetical phase space of the $sCA_{\gamma,d}$. The curve $d = d_c(\gamma)$ represents the unknown critical line of the sCA. sCA is unphysical beyond $\gamma = 4/3$ (stippled area).**

https://doi.org/10.5194/egusphere-2026-2469
Preprint. Discussion started: 22 May 2026

Interestingly the ζ_A estimates from the clusters simulated by a tropical-band model in T21 over Indian Ocean and Atlantic Ocean are close to that of the CA clusters (c.f. Table 1 of T21 and Table 1 here) which suggests that the modelled rain clusters may behave like percolating clusters, at least over the Indian Ocean and tropical Atlantic. Peters et al., (2009) analysis of observed rain clusters suggests a ζ_A is close to the percolation value as well. However, more effort are needed to elucidate the reasons behind the discrepancy between the ζ_A estimates from observation reported by T17 and Peter et al., (2009) to ascertain which value is more representative of the actual exponent. The distributions of the modeled rain clusters size for all tropical oceanic regions that include the spanning clusters in the data samples show a "bump" at the large cluster sizes (see Fig. 2 of T21), reminiscent the CA in the super critical region when d is no longer in the vicinity of d_c (c.f. Fig. 3).

The construction method and results from our CA model have implications to some recent studies on tropical rain clusters statistics. While Haerter (2019) focused on cold-pool dynamics of convective self-aggregation, the stochastic model they constructed simulated the effect of gravity currents away from the centre of precipitation cell with scale ~ 10–100 km, similar to the action of GW1 and GW2 in our model. However, cluster size statistics have not been explored in Haerter (2019). On the other hand, analysis of a range of dynamical models (from general circulation model to RCE models with different model settings) in Stephan and Stevens (2025) showed that large-scale vertical overturning (i.e., planetary and synoptic scale variability) is critical for rain cluster size statistics to follow power law. This might be related to the larger ζ_A over the Pacific Ocean compared with other oceanic regions obtained in T21. While such large-scale variability has not been represented in our CA model, our lattice cell interactions through GW1 and GW2 have provided an answer to one of the discussion questions raised by Stephan and Stevens (2025), namely, "is feedback from convection, i.e., generation of waves and vertical motions by condensation relevant for the relationship between atmospheric motion and the distribution of column water vapor (CWV, and associated cluster size statistics)".

Nevertheless, we have imposed the scaling relationship between cluster rain rate and size in our CA model (via β in Eq. 6). T21 has argued that β may be a more fundamental parameter than the individual scaling exponents for cluster rain and area (i.e., ζ_R and ζ_A) as β can be estimated through some fundamental mesoscale dynamical processes (convective heating, entrainment, updraught velocity). With only gravity wave effects implemented in our model, indeed we have obtained robustness of the ζ_R and ζ_A exponents under different coupling strength γ. A question for further research would then be to what extent such "reductionist" model of convection organization, with simple site coupling mechanism, can simulate the scaling relationship between cluster rain rate and size as a natural outcome, or even the crossover behaviour from $\beta=4/3$ to $\beta=1$ when a MCS grows in size. As a side note, Stephan and Stevens (2025) focused on comparing the scaling exponents of CWV "islands" cluster area (i.e., those above a certain water vapor threshold with triggering deep convection consideration) distributions with observations and high-resolution simulations (Li et al. 2022). CA models with CWV as the central ingredient, such as a few those we reviewed in the introduction, may be validated along that line of thought.

https://doi.org/10.5194/egusphere-2026-2469
Preprint. Discussion started: 22 May 2026

5 Summary

A cellular automaton (CA) representing convective organization in a radiative-convective equilibrium is presented. This CA is based only on a limited set physical processes governing tropical deep convection and their organization. The basic parameter in the model is the MSE difference between the boundary layer and that at upper level, measuring atmospheric instability. The physical processes include large-scale destabilization and convective cell interaction through horizontally propagating gravity waves, thus separating the driving (synoptic) and relaxation (convective) timescale. Both near-field destabilization and far-field stabilization by the propagating gravity waves are represented in the model. Moreover, the CA cluster rain rate is constrained so that the scaling for E($R|a$) (expected rain rate conditioned by rain area) is as observed.

For a broad range of an adjustable model parameter, γ, that controls the degree of stabilization and destabilization in the vicinity of a deep convection, the CA exhibits criticality is similar to a 2-dimensional percolation, under a critical value of large-scale destabilization of the atmosphere. The ζ_A and ζ_R in the CA are insensitive to the value of γ, estimated to be 2.003 ± 0.058 and 1.721 ± 0.067 respectively. The CA ζ_A is near the value expected for 2-dimensional site-percolation. The observed scaling relation between β, ζ_A and ζ_R (Eq. 3) is reproduced. The RCM rain clusters resemble the CA rain clusters in a super-critical state. The basin-wide rain clusters from the RCM could behave like the incipient infinite percolating clusters of the CA.

Despite the other critical exponents of the CA, namely the η_S and D_S, $S\in\{A, R\}$, which vary with γ, the robustness of ζ_S to variations in γ means that a cellular automata that can account for the observed $\zeta_A \approx 5/3$ may be realized, such as by tuning the stabilization / destabilization of the atmosphere by deep-convection induced gravity waves, and has the potential of exhibiting criticality and reproducing the observed $\zeta_A \approx 5/3$.

Appendix A

T17 and T21 investigated the scaling behavior of tropical oceanic rain clusters using the framework of SOC. The first study (T17) analyzed satellite rainfall observations (TRMM 3B42), while the second (T21) examined output from a Weather, Research and Forecast (WRF)-based regional climate model over the tropical band. Key concepts and scaling exponents are introduced below.

A.1 SOC and scaling laws

Under the SOC paradigm, tropical deep convection is hypothesized to self-organize into rain clusters of all sizes, analogous to avalanches in a critical sandpile. For a system at criticality, the probability distributions of cluster observables follow simple scaling:

$$f_S(s) \sim s^{-\zeta_S} \mathcal{G}_S\left(\frac{s}{s_c}\right), \qquad s > s_0;\ S \in \{A, R\} \tag{A1}$$

https://doi.org/10.5194/egusphere-2026-2469
Preprint. Discussion started: 22 May 2026

where S denotes either the cluster area A(in units of grid-cell area ΔA) or the total rain rate R(in units of $\Delta A \times 0.01$ mm/h), ζ_S is the scaling exponent, $\mathcal{G}_S$ is a finite-size scaling function, and ξ_S is an upper cutoff that increases with domain size. The power-law regime holds for $s_0 \ll s \ll \xi_S$.

A.2 Scaling exponents from observations

Using 15 years of TRMM 3B42 data over the Indo-Pacific warm pool and the intertropical convergence zones (ITCZ) of the eastern Pacific and Atlantic, T17 estimated the scaling exponents for $A$and R after accounting for domain-size dependence. The universal (basin-independent) values were found to be:

$$\zeta_A = 1.66 \pm 0.06\ (\sim 5/3),$$
$$\zeta_R = 1.48 \pm 0.13\ (\sim 3/2). \tag{A2}$$

Furthermore, the conditional mean of the cluster rain rate given its area, $\mathrm{E}(R \mid a)$, exhibited two distinct scaling regimes:

$$\mathrm{E}(R \mid a) \sim \begin{cases} a^{\beta} & a \le \alpha\ (mesoscale\ clusters) \\ a^{\chi} & a > \alpha (larger\ clusters), \end{cases} \tag{A3}$$

with $\beta = 1.33 \pm 0.03\ (\sim 4/3)$, $\chi = 0.97 \pm 0.04\ (\sim 1.0)$, and the crossover area α with associated length scale ~320 km. For mesoscale clusters ($\beta > 1$), growth is accompanied by intensification. While for larger clusters ($\chi \approx 1$), the average rain intensity saturates, suggesting that superclusters grow mainly by aggregation without further intensification. The exponents satisfy the SOC scaling relation:

$$\beta = \frac{(\zeta_A - 1)}{(\zeta_R - 1)} \tag{A4}$$

which holds for the observed values.

A.3 Scaling exponents from model output

T21 applied an identical methodology to 28 years of WRF model output (36 km resolution) over the same tropical ocean basins. The model rain clusters did not exhibit universality: the estimated $\zeta_A$and $\zeta_R$varied significantly across basins (e.g., ζ_A ranged from 2.12 ± 0.10 over the Indian Ocean to 2.48 ± 0.09 over the western Pacific). Moreover, the model failed to reproduce the crossover in $\mathrm{E}(R \mid a)$. Instead, a single power law $\mathrm{E}(R \mid a) \sim a^{\beta}$ held over the entire range of cluster sizes, with $\beta = 1.36 \pm 0.05$ (averaged across basins). This value agrees with the observed β for mesoscale clusters, indicating that the model captures the fundamental intensification dynamics of small-to-moderate clusters. However, the absence of the crossover (i.e., β remaining above unity for synoptic-scale clusters) and the unrealistic basin-wide rain bands produced by the model suggest that its large-scale convective organization departs from reality.

https://doi.org/10.5194/egusphere-2026-2469
Preprint. Discussion started: 22 May 2026

Appendix B

The CA uses the stability of the tropical atmosphere as a basis for the model variable. A schematic of the profile of the model h and h^* and various definitions are shown in Fig. B1 to aid the model description. Specifically, we adopt the Arakawa's penetrative convection (Schubert, 2000) for deep convection

$$h_1 > \left(h^*_{2,3}\right) > h_2 \tag{B1}$$

where h_1, h_2 and h_3 are the density-averaged of the boundary (1000mb – 850mb), middle (850mb – 450mb) and upper layer (100mb – 450mb) tropospheric specific moist static energy. h^* is the density-averaged saturated moist static energy. Note that $h_1 = h_1(x, y, t)$, where (x, y) is the coordinates of a location on the surface and t is the time. Similar functional dependence for the rest of the layer-averaged parameters. From typical vertical profiles of the observed moist static energy found in the literature (e.g. Emanuel, 1994), it is reasonable to assume $h^*_3 \approx h^*_2 (> h_2)$ which simplifies the condition for deep convection to occur (Eq. B1) to

$$X > 0 \tag{B2}$$

where $X \stackrel{\text{def}}{\equiv} h_1 - h^*_3$ is the primary variable of the CA. In the CA, the atmosphere is stable against deep (moist) convection when $X < 0$ and is defined to be bounded below by say, X_0 (< 0), representing the notion that the atmosphere has a maximum stability attainable. From here on, all variables in the CA having the same units of X is understood to be normalized by $|X_0|$. Hence $X \geq$ -1 in the CA.

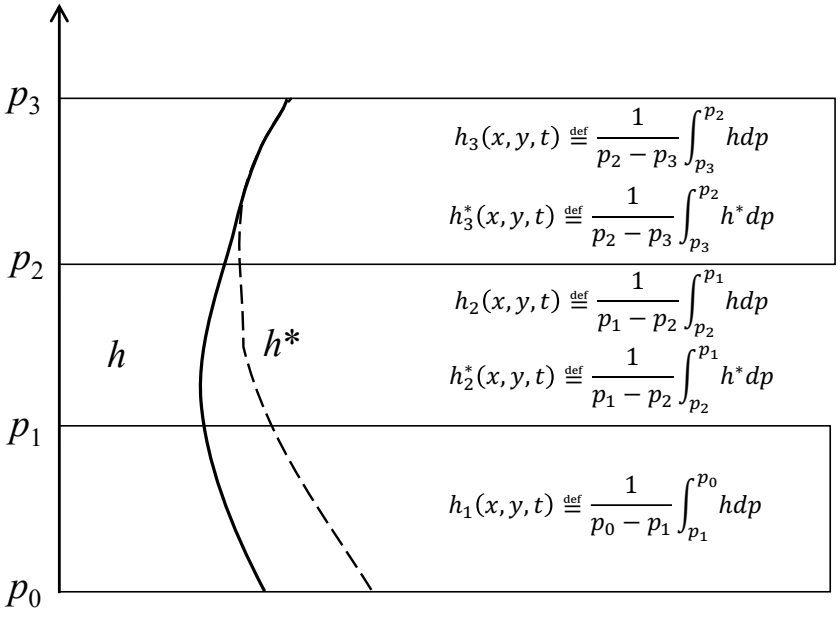

Figure B1: Illustration of the moist static energy profiles in the CA. Vertical axis is the atmospheric pressure.

https://doi.org/10.5194/egusphere-2026-2469
Preprint. Discussion started: 22 May 2026

B.1 Large-scale destabilisation (Eq. 1)

We assume that the large scale moist static energy at the boundary layer to be the net result of the radiative fluxes and the latent and sensible heat fluxes at the surface provide the large scale forcing. At the upper troposphere, the moist static energy is assumed to change in response to the net radiative fluxes only. Changes of the moist static energy as a result of large scale vertical and horizontal advection is not considered in the CA. By assuming that the time rate of change of h_3^* is the same as the rate of change of h_3,

$$\dot{X}_{LS} = F_1 + E_1 - E_3 \tag{B3}$$

where $\dot{X}_{LS}$ is the large-scale rate of change of X (e.g. the spatial-temporal averages of dX/dt across the domain, and over a time interval, τ_{LS}, much longer than the convective timescale); E_1 and E_3 the rate of large-scale heating from radiation at the boundary layer and upper tropospheric layer respectively; F_1 the large-scale heating rate due to the latent and sensible heat fluxes. Typical value for the rhs of Eq. (A3) for the tropical atmosphere estimated from existing literature are as follows: $F_1 \approx 6.774$ kJkg^{-1}day^{-1}, $E_1 \approx -1012$ Jkg^{-1}day^{-1} and $E_3 \approx -1006$ Jkg^{-1}day^{-1}. Hence $\dot{X}_{LS} \approx 5.768$ kJkg^{-1}day^{-1}, which means that the large scale forcing drives the tropical atmosphere towards instability. The amount of instability added in the CA at each lattice site, in a large-scale (or outer) time step, is

$$d = \dot{X}_{LS}\tau_{LS} > 0 \tag{B4}$$

B.2 Local effects of a deep convection process (Eqs. 2–4 in Table 1)

At the site where deep convection occurs, deep convection is assumed to transport the moist static energy from the boundary layer into the upper troposphere, thereby increasing h_3 and h_3^* under the simplifying assumption that the upper tropospheric layer is nearly saturated. At the same time, the compensating downdraft transports the low-h air from the mid troposphere into the boundary layer decreasing h_1. Therefore, the deep convection process decreases X at the site where the deep convection happens, stabilising the atmospheric column above the site. The amount of stabilisation

$$\Delta X_c \stackrel{\text{def}}{=} X_f - X_i \leq 0 \tag{B5}$$

where the i and f subscript denotes before and after convection. In the CA, the value X_f is a random variable with a probability distribution, $g(X_f)$, to reflect the stochasticity in the deep moist convection due to the entrainment and detrainment of cloudy and sub-saturated environmental air that affects how much of the local instability has been removed by the deep convection. The distribution, $g(X_f)$, is shown in Fig. B2. This distribution is estimated as follows: By making a crude assumption that X_f is proportional to the column precipitable water, W, in the column of air after the deep convection, we exploit the observations by Peters and Neelin (2006) by estimating the frequency of non-rainy instances given at different W (the differences between

https://doi.org/10.5194/egusphere-2026-2469
Preprint. Discussion started: 22 May 2026

number of occurrences for a given w (rainy and non-rainy) minus the number of occurrences for a given w which are rainy from their Fig. 3).

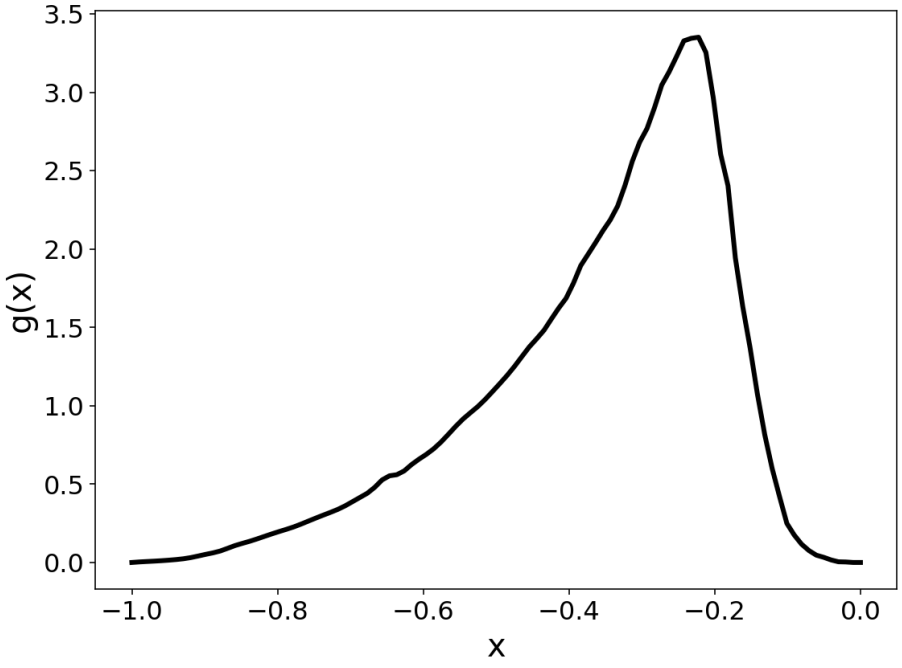

Figure B2: The distribution for X_f.

B.3 Effects of gravity waves excited by deep convection (Eq. 5 in Table 1)

Gravity waves effects have long been recognized as an important mechanism for convection clustering (Randall and Huffman 1980; Mapes 1993). The CA assumes that a deep convection event has a top heavy latent heating profile at the convecting site which is a linear combination of two modes of heating profiles, Q_1 and Q_2, with vertical wavenumbers ℓ =1 and ℓ =2 (the vertical wavelength is $2H/\ell$, H being the scale height of the deep convection). Referring to the schematics in Fig. B3, the horizontal gravity bores radiates outwards from the convecting site with a circular wave front with phase speed of $c_\ell \approx NH/(\ell\pi)$, N being the buoyancy frequency (Nicholls *et al.*, 1991). In the lifetime of the deep convection, τ_c ($\ll \tau_{LS}$), the two gravity bores GW1 and GW2 have moved a distance $r_\ell = c_\ell \tau_c$ away from the convective site, with $r_1 = 2r_2$.

The following assumptions are made 1) the flow is hydrostatic, incompressible and the motions outside the convective core to be adiabatic; 2) the horizontal transport of moist static energies is negligible when compare to the vertical transport of the moist static energies; 3) $h \approx h^*$ for $p > p_2$, except near the tropopause, where the vertical velocity drops quickly to zero, h^* is near constant within the upper tropospheric layer (see Fig. B1); 4) the pressure levels defining the boundary and upper tropospheric layers are approximately constant. Then

https://doi.org/10.5194/egusphere-2026-2469
Preprint. Discussion started: 22 May 2026

$$\frac{\partial h_1}{\partial t} = -\frac{1}{p_0 - p_1}\int_{p_1}^{p_0} \omega \frac{\partial h}{\partial z} dz = -\omega(p')\frac{\partial h}{\partial p}\Big|_{p=p'}; p_1 \le p' \le p_0,$$

where ω is the vertical velocity in pressure coordinates. Also,

$$\frac{\partial h_3^*}{\partial t} = -\frac{1}{p_2 - p_3}\int_{p_3}^{p_2} \omega \frac{\partial h^*}{\partial p} dp,$$

where the term $\omega \frac{\partial h^*}{\partial p}$ is small such that $\left|\frac{\partial h_1}{\partial t}\right| \gg \left|\frac{\partial h_3^*}{\partial t}\right|$. Hence,

$$\frac{\partial X}{\partial t} \approx \frac{\partial h_1}{\partial t} = -\omega(p')\frac{\partial h}{\partial p}\Big|_{p=p'}, p_1 \le p' \le p_0.$$

Rewriting $\omega(p)\frac{\partial h}{\partial p}\Big|_{p=p'}$ as $(\omega_1 + \omega_2)\left(\frac{\partial h}{\partial p}\right)_b$, where ω_ℓ is the averaged vertical velocity in pressure coordinates at the top of the boundary layer ($p = p_1$) due to the GWℓ (ℓ = 1,2) behind its wavefront (see below), and $\left(\frac{\partial h}{\partial p}\right)_b$, a representation of the effective vertical gradient of h in the boundary layer, the change of stabilisation due to GWℓ at the non-precipitating sites behind the gravity bore's wavefront due to the convection, ΔX_ℓ, is

$$\Delta X_\ell = -\omega_\ell \left(\frac{\partial h}{\partial p}\right)_b \tau_c; \quad \ell = 1,2 \tag{B6}$$

Since $\left(\frac{\partial h}{\partial p}\right)_b > 0$, GW1 stabilizes the atmosphere (i.e. $\Delta X_\ell < 0$) since $\omega_1 > 0$, while GW2 destabilizes the atmosphere since $\omega_2 < 0$ (see Fig. B3). The destabilizing effects due to the GW2 bore is in line with Mapes (1993) where the combined effects of the two gravity bores can destabilise the atmosphere by decreasing the convective inhibition at the vicinity of a deep convection through boundary layer convergence behind the GW2 bore.

Due to the incompressibility of the flow, the volume and time average

$$\iiint_V \int_0^{\tau_c} (\nabla \cdot \boldsymbol{u_\ell}) dt dv = 0\,; \ \ell = 1,2 \tag{B7}$$

where $\boldsymbol{u_\ell}$ is the velocity of the flow in response to the heating profile Q_ℓ and V is the cylindrical volume with a pressure thickness from p_1 to p_0, and with its centre at the convecting site and a radius just outside the GWℓ (ℓ=1,2) wavefront. Using the divergence theorem, we obtain from Eq. (B7):

$$\omega_\ell \approx -\frac{a_c}{A_\ell}\omega_{c\ell} \tag{B8}$$

where a_c is the area covered by the deep convection, A_ℓ the area outside the convection but behind the GWℓ wavefront, which is the area of an annulus with an inner radius $r_c = \sqrt{a_c/\pi}$ and an outer radius $c_1\tau_c$ (see Fig. B3); $\omega_{c\ell}$ the averaged vertical velocity of the deep convection site at the top of the boundary layer (averaged over a_c and time interval $0 \le t \le \tau_c$); w_ℓ the averaged vertical velocity due to GWℓ for sites within the annulus area A_ℓ at $p = p_1$ (averaged over A_ℓ and time interval $0 \le t \le \tau_c$). Since $|\omega_{c\ell}|$ is proportional to $|Q_\ell|$ which in turn is assumed to be proportional to $|\Delta X_c|$, we have (from Eqs. B6 and B8):

https://doi.org/10.5194/egusphere-2026-2469
Preprint. Discussion started: 22 May 2026

$$\Delta X_1 = \gamma_1 \Delta X_c;\ \ \gamma_1 > 0 \tag{B9}$$

$$\Delta X_2 = -\gamma_2 \Delta X_c;\ \ \gamma_2 > 0 \tag{B10}$$

where γ_1 and γ_2 are positive constants which are not are not independent since they are related to the relative magnitude between Q_1 and Q_2. By defining the ratio

$$\alpha \stackrel{\text{def}}{=} -\frac{\omega_{c2}}{\omega_{c1}} > 0 \tag{B11}$$

it is easy to show, using Eqs. (B6, B8 – B10), that

$$\frac{\gamma_2}{\gamma_1} = \frac{A_1}{A_2}\alpha \tag{B12}$$

We estimate α from literature by first noting that $\alpha = \frac{L_2}{L_1}$, where L_1 and L_2 are the amplitudes of the latent heating profile that excite the GW1 and GW2 assuming that the latent heating is balance by adiabatic ascent. We approximate that the total heating profile from deep convection as a linear combination of two sinusoids:

$$Q(z) = L_1 sin\left(\frac{\pi z}{H}\right) - L_2 sin\left(\frac{2\pi z}{H}\right) \tag{B13}$$

We use the vertical latent heating profile over the Tropical Western Pacific inferred from satellite cloud data by Jakob and Schumacher (2008) to estimate L_1 and L_2. The two turning points in their inferred profile in their Figure 4-3 is about (7 km, 1.38 Kday^{-1}) and (1 km, -0.13 Kday^{-1}), hence substituting the two co-ordinates into Eq. (B13) and taking H = 14 km and obtained a value of 0.75 for α.

In the CA with a square lattice, the sites behind the GW1 and GW2 wavefronts are taken to be nearest-neighbours and the next-nearest-neighbours (12 lattice sites) and the nearest-neighbours respectively (4 sites). Hence in the CA, $A_1 = 12a_c$ and $A_2 = 4a_c$. From Eq. (B12) we have $\gamma_2 = \frac{9}{4}\gamma_1$. For notational convenience, we defined $\gamma = 12\gamma_1$, hence $\gamma_2 = \frac{3}{16}\gamma$.

https://doi.org/10.5194/egusphere-2026-2469
Preprint. Discussion started: 22 May 2026

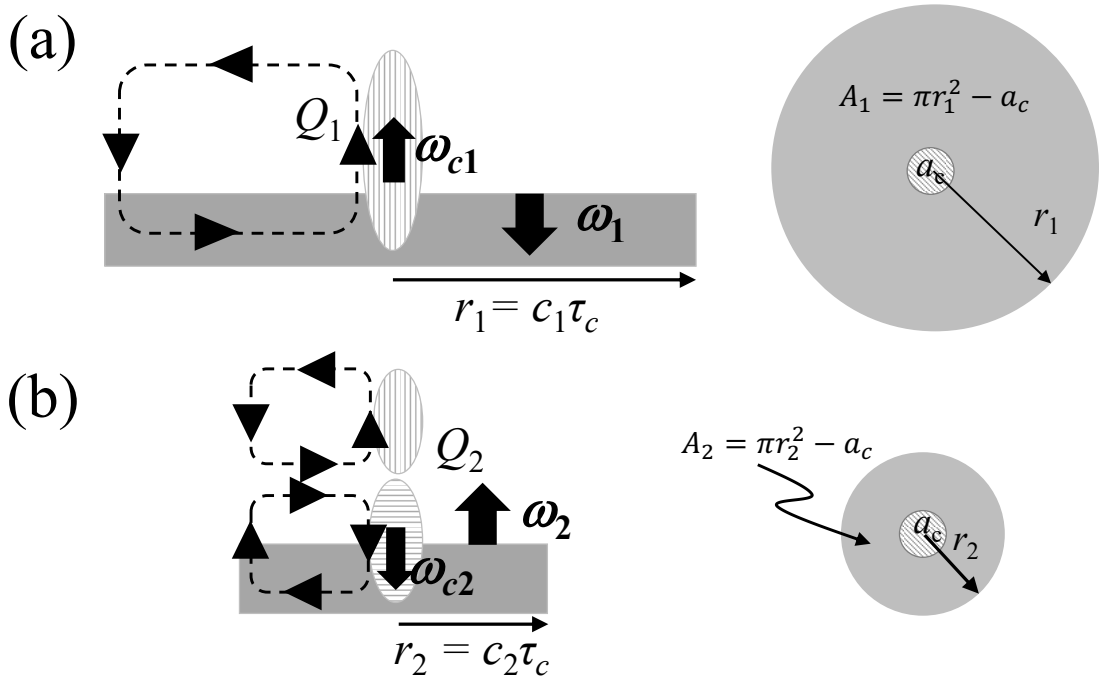

Figure B3: Schematic showing the effects on the atmosphere due to the (a) GW1 (ℓ = 1) and (b) GW2 (ℓ = 2) gravity bores. The diagrams on the left represent a vertical cross-section of the troposphere that includes the convective site. The vertical (horizontal) stippled ellipse at the middle of the figure represents a positive (negative) heating anomaly. The greyed region is a cross section of the volume of clear sky atmosphere within the sub cloud layer behind the wave fronts at a time τ_c. ω_1 and ω_2 are the area-time averaged velocities in the clear sky region behind the wave fronts (greyed region) due to the heating mode Q_1 and Q_2. The averaging is done over the area on the top of the boundary layer (top of the greyed area) and across time from the time convection is triggered to a duration τ_c. ω_{c1} and ω_{c2} are the area-time averaged vertical velocity confined within the convective site. The area averaging is done across the convective site only in this case. The cross-section of the instantaneous (radially symmetric) circulation at time τ_c after the convection is triggered is represented by the dotted loops with arrow indicating the direction of the circulation. The diagrams on the right represents the top view of the corresponding cross section views.

Appendix C

As we can obtain rain cluster distributions with well separated characteristic cluster length scales using the CA, we are able to probe the finite size scaling through moment analysis and data collapse to obtain the various scaling exponents for the distribution. In our following discussion all hatted symbols denote the estimates from the sample rain cluster distributions.

C.1 Estimating ζ_S

The finite scaling ansatz holds as well

When the distribution is finite-size scaling ($1 \ll Z \ll \xi_A$; Eq. 7), the analysis of moments is used to estimate ζ_S, $S \in \{A,R\}$. It can be shown that finite-size scaling requires the n^{th} moments of S (Prussner, 2012) to scales as follows:

https://doi.org/10.5194/egusphere-2026-2469
Preprint. Discussion started: 22 May 2026

$$\langle S^n \rangle \propto S_\xi^{\sigma_n^{(S)}}, \quad n > \zeta_S - 1 \tag{C1}$$

where S_ξ is the characteristic scale of S, which is in principal proportional to Z^{D_S}, and

$$\sigma_n^{(S)} = 1 + n - \zeta_S \tag{C2}$$

We estimate $S_\xi(Z)$ by dividing the third moment with the second moment of S for each Z (64, 128, 256, 512). For each n (equals to 2, 3, 4, 5), $\hat{\sigma}_n^{(S)}$, is first estimated from Eq. (C1) as the gradient of the linear regression of $\log\langle S^n \rangle$ against $\log S_\xi$. Finally, $\hat{\zeta}_S$ is estimated using another linear regression of $\hat{\sigma}_n^{(S)}$ against n, following Eq. (C2). The 95% confidence interval of the intercept estimates is adopted as the error for $\hat{\zeta}_S$.

When $\xi_S \ll Z$, we observe that the resulting point estimates for ζ_S from the moment analysis described above are generally sub-optimal; the data collapse using the ζ_S estimates from moment analysis does not collapse well. Preliminary trial-and-error for a few cases show that better point estimate for ζ_S can result in better data collapse. We suspect that finite domain effects may still be significant when $\xi_S \ll Z$ rendering the moment scaling relation of Eq. (C1) accurate only for domain sizes beyond $Z = 512$. As such we use an objective data collapse method to estimate ζ_S for $\xi_S \ll Z$. This method exploit the fact that in an ideal data collapse, $M_S(\zeta_S, d) \stackrel{\text{def}}{=} \max_s s^{\tau_S} f_S(s; d)$, where $f_S(s;d)$ is the probability distribution for S when an external drive d is applied on the CA (for a given γ), is identical across all d. The method of the objective data collapse is outlined as follows: For each $\hat{\zeta}_S \in [a, b]$, calculate $M_S(\hat{\zeta}_S, d_j)$ for every d_j (e.g. $d_j = 0.25, 0.26, 0.27, 0.28$ for the $CA_{0,d}$; see Figure 9a in the main text) and then obtain the sample variance from the set $\{\ln M_S(\hat{\zeta}_S, d_j) \mid j = 1,2,..\}$. The $\hat{\zeta}_S$ that gives the minimum sample variance (and hence the best data collapse out of all the exponent tested) is identified as the best estimate for ζ_S. In our work, $[a, b]$ is an interval covering the range of the likely ζ_S.

The error for $\hat{\zeta}_S$ due to the uncertainty in sampling the probability distribution can be shown to be

$$\delta\hat{\zeta}_S \approx \frac{1}{B}\sum_{j=1}^{J} \left|\ln s_j^* - \overline{\ln s^*}\right| \left|\delta F_j^{(S)}\right| \tag{C3}$$

where $s_j^{*\hat{\zeta}_S} \hat{f}_S(s_j^*; d_j) = M_S(\hat{\zeta}_S, d_j)$; $\overline{\ln s^*} = \sum_j \ln s_j^* / J$; $B = \sum_{j=1}^{J} \left(\ln s_j^* - \overline{\ln s^*}\right)^2$; $\delta F_j^{(S)} = \ln\left[\hat{f}_S(s_j^*; d_j) + \delta f_S^*\right] - \ln \hat{f}_S(s_j^*; d_j)$, δf_S^* being the error of sample probability distribution $\hat{f}_S(s_j^*; d_j)$. We estimate δf_S^* as follows: Define $p^* = P(s_1 \le S < s_2)$ where $I = [s_1, s_2)$ is the bin interval containing s_j^* and note that the number of clusters out of a total of N clusters that would have s falling within I follows a binomial distribution. For large enough N as in our work, the 95% confidence interval for the estimates for p^* is $\hat{p}^* \pm \sigma^*$, where $\hat{p}^*$ is our binomial proportion estimate for p^* and $\sigma^* = 1.96\sqrt{\hat{p}^*(1-\hat{p}^*)/N}$. δf_S^* is then estimated as $\sigma^*/\|I\|$ where $\|I\| = |s_2 - s_1|$ if S is R, or $\|I\|$ is the number of integers containing within the interval I if S is A. The estimate for ζ_S presented in the main text (Table 2 and Fig. 6a) is the average estimates from the above two different methods.

https://doi.org/10.5194/egusphere-2026-2469
Preprint. Discussion started: 22 May 2026

C.2 Estimating D_S, η_S and d_c

When the distribution is finite-size scaling, we obtain D_S as the regression slope of the characteristic scale S_0 against Z (see above) and the 95% confidence interval of the regression slope taken as the error of D_S.

When $\xi_S \ll Z$, $S_0 \propto |d - d_c(\gamma)|^{-\eta_S}$ (Eq. 8 in the main text). For a given γ, S_0 is obtained from the cluster data as described earlier. For each $d_c^* \in [a, b]$, where $[a, b]$ is a prescribed interval which contains the potential $\hat{d}_c$, linear regression of log S_0 against $\log|d - d_c^*|$ is performed. The d_c^* whose regression has the minimum root-mean square error is taken to be the best estimate for d_c and the corresponding regression slope is the best estimates for $\underline{\eta_S}$. The 95% confidence of the regression slope is taken as the error for $\hat{\eta}_S$.

Code and data availability

Codes and generated datasets from this study can be obtained from the authors upon reasonable requests.

Author contributions

KKWC, CKT and TYK conceived the study and designed the experiments. CKT developed the model code, performed the simulations and data analyses. KKWC and CKT prepared the draft manuscript. All co-authors contributed to interpretation of results, manuscript revision and its finalization.

Competing interests

The authors declare no conflicts of interest.

Disclaimer

Copernicus Publications adds a standard disclaimer: “Copernicus Publications remains neutral with regard to jurisdictional claims made in the text, published maps, institutional affiliations, or any other geographical representation in this paper. While Copernicus Publications makes every effort to include appropriate place names, the final responsibility lies with the authors. Views expressed in the text are those of the authors and do not necessarily reflect the views of the publisher.”

Please feel free to add disclaimer text at your choice, if applicable.

https://doi.org/10.5194/egusphere-2026-2469
Preprint. Discussion started: 22 May 2026

Acknowledgements

KKWC acknowledges support from The Startup Foundation for Introducing Talent of the Nanjing University of Information Science and Technology.

Financial support

This study receives no financial support.

Review statement

The review statement will be added by Copernicus Publications listing the handling editor as well as all contributing referees according to their status anonymous or identified.

References

Bak, P., Tang, C., Wiesenfeld, K.: Self-organized criticality: An explanation of the 1/f noise, Phys. Rev. Lett., 59, 381, https://doi.org/10.1103/PhysRevLett.59.381, 1987.

Bao, J., Sherwood, S., Colin, M., Dixit, V.: The Robust Relationship Between Extreme Precipitation and Convective Organization in Idealized Numerical Modeling Simulations. J. Adv. Modeling Earth Syst., 9, 2291–2303, doi:/10.1002/2017MS001125, 2017.

Bengtsson, L., Gerard, L., Han, L., Gehne, M., Li, W., Dias, J.: A prognostic-stochastic and scale-adaptive cumulus convection closure for improved tropical variability and convective gray-zone representation in NOAA's Unified Forecast System (UFS). Mon. Wea. Rev., 150, 3211–3227, doi:/10.1175/MWR-D-22-0114.1, 2022.

Broadbent, S., Hammersley, J.: Percolation processes: I. Crystals and mazes. Math. Proc. Cambridge Phil. Soc., 53, 629–641, https://doi.org/doi:10.1017/S0305004100032680, 1957.

Bröker, H. M., Grassberger, P.: Random neighbor theory of the Olami-Feder-Christensen earthquake model. Phys. Rev. E, 56, 3944, https://doi.org/10.1103/PhysRevE.56.3944, 1997.

Cahalan, R. F., Joseph, J. H.: Fractal statistics of cloud fields, Mon. Wea. Rev., 117, 261–272, https://doi.org/10.1175/1520-0493(1989)117<0261:FSOCF>2.0.CO;2, 1989.

Cerlini, P., Saraceni, M., Silvestri, L.: Competing Effect of Radiative and Moisture Feedback in Convective Aggregation States in Two CRMs. J. Adv. Modeling Earth Syst., 13, doi:/10.1029/2022MS003323, 2023.

Chabanol, M. L., Hakim, V.: Analysis of a dissipative model of self-organized criticality with random neighbors. Phys. Rev. E, 56, R2343, https://doi.org/10.1103/PhysRevE.56.R2343, 1997.

Cheraghalizadeh, J., Luković, M., Najafi, M. N.: Simulating cumulus clouds based on self-organized criticality. Physica A, 636, 129553, https://doi.org/10.1016/j.physa.2024.129553, 2024.

Christensen, K., Moloney, N. R.: Complexity and Criticality, Imperial College Press, London, U.K., 2005.

De Carvalho, J. X., Prado, C. P.: Self-organized criticality in the Olami-Feder-Christensen model. Phys. Rev. Letts., 84, 4006, https://doi.org/10.1103/PhysRevLett.84.4006, 2000.

Devineni, N., Lall, U., Xi, C., Ward, P.: Scaling of extreme rainfall areas at a planetary scale. Chaos, 25, 075407, https://doi.org/10.1063/1.4921719, 2015.

Dickman, R., Vespignani, A., Zapperi, S.: Self-organized criticality as an absorbing-state phase transition. Phys. Rev. E, 57, 5095, https://doi.org/10.1103/PhysRevE.57.5095, 1998.

Emanuel, K. A.: Atmospheric Convection. Oxford University Press, U.K., 1994.

https://doi.org/10.5194/egusphere-2026-2469
Preprint. Discussion started: 22 May 2026

Graf, H., Yang, J.: Evaluation of a new corrective cloud field model: Precipitation over the maritime continent. Atmos. Chem. Phys., 7, 409–421, https://doi.org/10.5194/acp-7-409-2007, 2007.
Haerter, J. O.: Convective self-aggregation as a cold pool-driven critical phenomenon. Geophys. Res. Lett., 46, 4017–4028, https://doi.org/10.1029/2018GL081817, 2019.
Jakob, C., Schumacher, C.: Precipitation and latent heating characteristics of the major tropical western Pacific cloud regimes. J. Climate, 21, 4348–4364, https://doi.org/10.1175/2008JCLI2122.1 2008.
Li, Y., Yano, J., Lin, Y.: Is atmospheric convection organized? Information entropy analysis. Geophys. Astrophys. Fluid Dyna., 113, 553–573, https://doi.org/10.1080/03091929.2018.1506449, 2019.
Li, Z., O'Gorman, P. A., Rothman, D. H.: Tropical precipitation clusters, as islands on a rough water-vapor topography. Quart. J. Roy. Meteorol. Soc., 148, 403–417, 2022.
López, R. E.: The Lognormal Distribution and Cumulus Cloud Populations. Mon. Wea. Rev., 105, 865–872, https://doi.org/10.1175/1520-0493(1977)105<0865:TLDACC>2.0.CO;2, 1977.
López, R. E.: Internal Structure and Development Processes of C-Scale Aggregates of Cumulus Clouds. Mon. Wea. Rev., 106, 1488–1494, https://doi.org/10.1175/1520-0493(1978)106<1488:ISADPO>2.0.CO;2, 1978.
Lovejoy, S.: Area–perimeter relation for rain and cloud areas. Science, 216, 185–187, https://doi.org/10.1126/SCIENCE.216.4542.185, 1982.
Malamud, B. D., Turcotte, D. L.: Cellular-automata models applied to natural hazards. IEEE Computing in Science and Engineering, 2, 42–51, doi:/10.1109/5992.841795, 2000.
Mapes, B. E.: Gregarious tropical convection, J. Atmos. Sci., 50, 2026–2037, https://doi.org/10.1175/1520-0469(1993)050<2026:GTC>2.0.CO;2, 1993.
Muller, C., J., Romps, D.: Acceleration of tropical cyclogenesis by self-aggregation feedbacks. Proc. Nat. Acad. Sci., 115, 2930–2935, https://doi.org/10.1073/pnas.1719967115, 2018.
Muller, C. J., Back, L. E., O'Gorman, P. A., Emanuel, K. A.: A model for the relationship between tropical precipitation and column water vapor. Geophys. Res. Letts., 36, https://doi.org/10.1029/2009GL039667, 2009.
Nagel, K., Raschke, E.: Self-organizing criticality in cloud formation? Physica A, 182, 519–531, https://doi.org/10.1016/0378-4371(92)90018-L, 1992.
Najafi, M. N., Cheraghalizadeh, J., Herrmann, H. J.: Self-organized criticality in cumulus clouds. Phys. Rev. E, 103, 052106, https://doi.org/10.1103/PhysRevE.103.052106, 2021.
Neggers, R. A. J., Groewank, P., Heus, T.: Power-law scaling in the internal variability of cumulus cloud size distributions due to subsampling and spatial organization. J. Atmos. Sci., 76, 1489–1503, https://doi.org/10.1175/JAS-D-18-0194.1, 2019.
Nicholls, M. E., Pielke, R. A., Cotton, W. R.: Thermally forced gravity waves in an atmosphere at rest. J. Atmos. Sci., 48, 1869–1884, https://doi.org/10.1175/1520-0469(1991)048<1869:TFGWIA>2.0.CO;2 1991.
Nober, F., Graf, H.: A new convective cloud field model based on principles of self-organisation. Atmos. Chem. Phys., 5, 2749–2759, https://doi.org/10.5194/acp-5-2749-2005, 2005.
O'Brien, T. A., Li, F., Collins, W. D., Rauscher, S. A., Ringler, T. D., Taylor, M., Hagos, S. M., Leung, L. R.: Observed scaling in clouds and precipitation and scale incognizance in regional to global atmospheric models. J. Climate, 26, 9313–9333, 2013.
Olami, Z., Feder, H. J. S., Christensen, K.: Self-organized criticality in a continuous, nonconservative cellular automaton modeling earthquakes. Phys. Rev. Letts., 68, 1244, https://doi.org/10.1103/PhysRevLett.68.1244, 1992.
Otsuka, S., Trilaksono, N.J., Yoden, S.: Comparing simulated size distributions of precipitation systems at different model resolution. SOLA, 13, 130–134, https://doi.org/10.2151/sola.2017-024, 2017.
Palmer, T. N.: On parametrizing scales that are only somewhat smaller than the smallest resolved scales, with application to convection and orography. Proceedings of the 1996 ECMWF workshop on convection, ECMWF, Shinfield Park, Reading, UK, 1997.
Palmer, T. N.: A nonlinear dynamical perspective on model error: A proposal for non-local stochastic-dynamic parametrization in weather and climate prediction models. Quart. J. Roy. Meteorol. Soc., 127, 279–304, https://doi.org/10.1002/QJ.49712757202, 2001.
Pendergrass, A.: Changing degree of convective organization as a mechanism for dynamic changes in extreme precipitation. Curr. Clim. Change Rep., 6, 47–54, https://doi.org/10.1007/s40641-020-00157-9, 2020.

https://doi.org/10.5194/egusphere-2026-2469
Preprint. Discussion started: 22 May 2026

Peters, O., Neelin, J. D.: Critical phenomena in atmospheric precipitation, Nature Phys., 2, 393–396, https://doi.org/10.1038/nphys314, 2006.
Peters, O., Neelin, J. D., Nesbitt, S. W.: Mesoscale convective systems and critical clusters, J. Atmos. Sci., 66, 2913–2924, https://doi.org/10.1175/2008JAS2761.1, 2009.
Peters, O., Deluca, A., Corral, Á., Neelin, J. D., Holloway, C. E.: Universality of rain event size distributions, J. Stat. Mech. Theor. Exp., 2010, P11030, https://doi.org10.1088/1742-5468/2010/11/P11030, 2010.
Piegari, E., Cataudella, V., Di Maio, R., Milano, L., Nicodemi, M.: Finite driving rate and anisotropy effects in landslide modeling. Phys. Rev. E, 73, 026123, https://doi.org/10.1103/PhysRevE.73.026123, 2006.
Pruessner, G.: Self-Organised Criticality: Theory, Models and Characterisation. Cambridge University Press, 2012.
Randall, D., Huffman, G.: A stochastic model of cumulus clumping. J. Atmos. Sci., 37, 2068–2078, https://doi.org/10.1175/1520-0469(1980)037<2068:ASMOCC>2.0.CO;2, 1980.
Roca, R., Fiolleau, T.: Extreme precipitation in the tropics is closely associated with long-lived convective systems. Comm. Earth Env., 1, https://doi.org/10.1038/S43247-020-00015-4, 2020.
Savre, J., Craig, G.: Fitting cumulus cloud size distributions from idealized cloud resolving model simulations. J. Adv. Mod. Earth Syst., 15, https://doi.org/10.1029/2022MS003360, 2023.
Schubert, W.: A Retrospective View of Arakawa's Ideas on Cumulus Parameterisation. In D. Randall (Eds.), General Circulation Model Development: Past, Present and Future, pp.181 – 198, Academic Press, 2000.
Semie, A., Bony, S.: Relationship between precipitation extremes and convective organization inferred from satellite observations. Geophys. Res. Lett., 47, https://doi.org/10.1029/2019GL086927, 2020.
Silva, A. R., Silva, A. R., Gouvêa, M. M.: A novel model to simulate cloud dynamics with cellular automaton. Env. Modeling & Software, 122, 104537, https://doi.org/10.1016/j.envsoft.2019.104537, 2019.
Stauffer, D., Aharony, A.: Introduction to Percolation Theory, 2 revised edition, Taylor & Francis, 1994, 181 pp.
Stechmann, S. N., Neelin, J. D.: First-passage-time prototypes for precipitation statistics. J. Atmos. Sci., 71, 3269–3291, 10.1175/JAS-D-13-0268.1, 2014.
Stephen, C. C., Stevens, B.: Dynamical imprints on precipitation cluster statistics across a hierarchy of high-resolution simulations. Atmos. Chem. Phys., 25, 1209–1226, https://doi.org/10.5194/ACP-25-1209-2025, 2025.
Teo, C.-K., Huynh, H.-N., Koh, T.-Y., Cheung, K. K. W., Legras, B., Chew, L. Y., Norford, L.: The universal scaling characteristics of tropical oceanic rain clusters, J. Geophys. Res. Atmos., 122, 5582–5599, https://doi.org/doi:10.1002/2016JD025921, 2017.
Teo, C.-K., Koh, T.-Y., Cheung, K. K. W., Legras, B., Huynh, H.-N., Chew, L.-Y., Norford, L., Scaling characteristics of modelled tropical oceanic rain clusters. Quart. J. Roy. Meteorol. Soc., 147, 1055–1069, https://doi.org/10.1002/qj.3959, 2021.
Traxl, D., N. Boers, A. Rheinwalt, B. Goswami, and J. Kurths (2016), The size distribution of spatiotemporal extreme rainfall clusters around the globe, Geophys. Res. Lett., 43(18), 9939-9947.
Vespignani, A., Zapperi, S.: How self-organized criticality works: A unified mean-field picture. Physical Review E, 57, 6345, https://doi.org/10.1103/PhysRevE.57.6345, 1998.
Wing, A. A., Emanuel, K.: Physical mechanisms controlling self-aggregation of convection in idealized numerical modeling simulations. J. Adv. Modeling Earth Syst., 6, 59–74, doi:/10.1002/2013MS000269, 2014.
Wing, A. A., Emanuel, K., Holloway, C. E., Muller, C.: Convective self-aggregation in numerical simulations: A review. In Pincus, R., Winker, D., Bony, S., Stevens, B. (eds) Shallow Clouds, Water Vapor, Circulation, and Climate Sensitivity. Space Sciences Series of ISSI, vol 65., Springer, Cham., https://doi.org/10.1007/978-3-319-77273-8_1, 2017.
Wood, R., Field, P. R.: The distribution of cloud horizontal sizes, J. Climate, 24, 4800-4816, 10.1175/2011JCLI4056.1, 2011.
Yao, L., Yang, D., Tan, Z.: A vertically resolved MSE framework highlights the role of the boundary layer in convective self-aggregation. J. Atmos. Sci., 79, 1615–1631, https://doi.org/10.1175/JAS-D-20-0254.1. 2022.
Zhang, Y., Wang, K.: Global precipitation system size. Env. Res. Lett., 16, 054005, https://doi.org/10.1088/1748-9326/abf394, 2021.